CellPress

Neuron
Primer

Visualizing Whole-Brain Activity and Development at the Single-Cell Level Using Light-Sheet Microscopy

Philipp J. Keller[1,*] and Misha B. Ahrens[1,*]
[1]Howard Hughes Medical Institute, Janelia Research Campus, 19700 Helix Drive, Ashburn, VA 20147, USA
*Correspondence: kellerp@janelia.hhmi.org (P.J.K.), ahrensm@janelia.hhmi.org (M.B.A.)
http://dx.doi.org/10.1016/j.neuron.2014.12.039

The nature of nervous system function and development is inherently global, since all components eventually influence one another. Networks communicate through dense synaptic, electric, and modulatory connections and develop through concurrent growth and interlinking of their neurons, processes, glia, and blood vessels. These factors drive the development of techniques capable of imaging neural signaling, anatomy, and developmental processes at ever-larger scales. Here, we discuss the nature of questions benefitting from large-scale imaging techniques and introduce recent applications. We focus on emerging light-sheet microscopy approaches, which are well suited for live imaging of large systems with high spatiotemporal resolution and over long periods of time. We also discuss computational methods suitable for extracting biological information from the resulting system-level image data sets. Together with new tools for reporting and manipulating neuronal activity and gene expression, these techniques promise new insights into the large-scale function and development of neural systems.

INTRODUCTION

Understanding brain function is challenging because the activity of all of its constituent cells is interdependent, creating an exceedingly complex dynamical system. In some cases where there is homogeneity among elements of a large system, physicists have been able to describe such joint dynamics in simplified terms, such as in models of gas molecules or magnetic interactions. Such simplifications are not possible in the nervous system because there is great heterogeneity between its components; for example, with respect to intracellular properties, synapse strength, and connectivity patterns. Nervous system development is similarly complex because it involves spatial and temporal cues that are generated within the system. A growing neurite behaves according to guidance cues from other cells, which are, in turn, dynamically affected by further spatiotemporally varying chemical fields and tissue geometries.

What is necessary for gaining an understanding of these systems? Given the global nature of both problems, it is useful to study these systems as a whole. This involves covering large spatial extents of the system with sufficient spatial resolution to identify many cells in the interrogated volume while maintaining sufficient temporal resolution to track the dynamics (the position, neural activity, or other properties) of these cells.

Optical imaging approaches, in combination with genetic tools and computational techniques, are starting to enable such global interrogations of the nervous system (Figure 1). In certain organisms of sufficiently small size, the coverage can even be close to complete. It is now possible to track almost every newly born and migrating brain cell and image the neural activity patterns of almost all neurons in animals such as the larval zebrafish. By focusing on larger volumes with these new techniques, the caveats associated with restricting the observations to small subvolumes of the nervous system are reduced.

In past decades, the development and function of living biological systems at microscopic scales has frequently been observed using point-scanning techniques (Figure 1A) or wide-field microscopes (Figure 1C). Although these approaches are invaluable for advancing our understanding of the nervous system (Grienberger and Konnerth, 2012; Grutzendler et al., 2002; Lichtman and Denk, 2011; Trachtenberg et al., 2002), their limitations impact the design of imaging experiments. Point-scanning imaging systems, such as confocal or two-photon microscopes, are capable of 3D optical sectioning and provide good spatial resolution, but their sequential, voxel-by-voxel scanning approach limits imaging speed. In confocal microscopy, the high light exposure of the specimen further limits long-term imaging capabilities. In contrast, conventional wide-field microscopes can deliver high imaging speeds through simultaneous acquisition of signal from many volume elements, but they cannot perform optical sectioning.

More recently, a fluorescence imaging technique has emerged that combines the distinct advantages of conventional techniques and effectively addresses previous limitations. Volumetric imaging assays based on this method, which is commonly referred to as light-sheet fluorescence microscopy, offer high imaging speed and good 3D spatial resolution. At the same time, they minimize the energy load on the specimen and, therefore, photobleaching and phototoxic effects (Figures 1E and 1F). These capabilities make light-sheet microscopes especially useful for live-imaging applications that require the observation of fast dynamic processes with high spatiotemporal resolution and over long periods of time, such as comprehensive

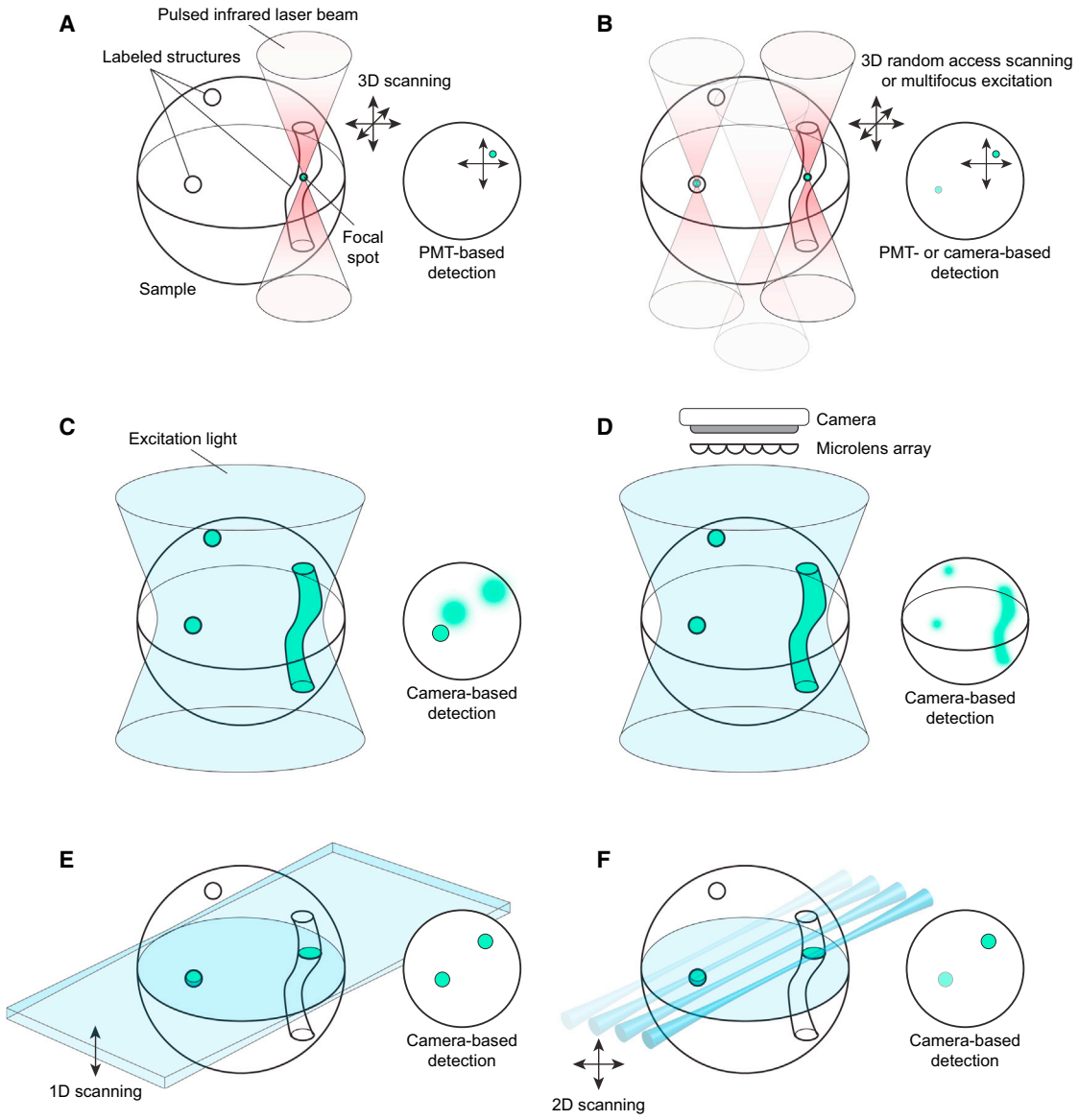

Figure 1. 3D Fluorescence Microscopy Methods

In each panel, the schematic on the left illustrates the illumination strategy, and the schematic on the right illustrates the fluorescence detection process.

(A) Point-scanning two-photon microscopy. A beam of laser light is focused into the specimen with a high numerical aperture objective (red light cone, representing light with infrared wavelengths) to excite fluorescent molecules in a small focal volume (green sphere). This focal spot is then scanned in one, two, or three dimensions, and fluorescence is measured at every coordinate with a photomultiplier tube (PMT) (Denk et al., 1990).

(B) Random-access and multifocus two-photon microscopy. The focal spot is rapidly moved in three dimensions—using, e.g., acousto-optic deflectors—to monitor different locations in the sample volume (Grewe et al., 2010; Katona et al., 2012). Alternatively, multiple focal spots can also be formed simultaneously, without the need for scanning (Anselmi et al., 2011; Nikolenko et al., 2008; Quirin et al., 2014).

(C) Wide field microscopy. The volume is bathed in excitation light with visible wavelengths (shown in blue), and a plane is imaged with a camera.

(D) Light-field microscopy. The entire sample is illuminated with excitation light. Emitted photons pass through light-field optics, and computational methods are used to reconstruct the volume (Broxton et al., 2013; Levoy et al., 2006, 2009; Prevedel et al., 2014).

(E) Light-sheet microscopy. A thin sheet of laser light is formed with a cylindrical lens to illuminate a single plane in the sample. Images are captured with a camera. For 3D imaging, the specimen is moved step by step relative to the light sheet (Fuchs et al., 2002; Huisken et al., 2004; Voie et al., 1993), or the light sheet and detection focal plane are moved across the sample volume (Holekamp et al., 2008; Planchon et al., 2011; Wu et al., 2011).

(F) Laser-scanning light-sheet microscopy. A micrometer-thin beam of laser light enters the sample from the side and is subjected to rapid 1D scanning to illuminate one plane (Keller et al., 2008). Emitted fluorescence light is detected with a camera. Rapid 3D imaging is performed by moving the illuminated plane and detection focal plane across the sample volume while keeping the sample stationary (Ahrens et al., 2013).

tracking of neural progenitors in the developing nervous system (Amat et al., 2014), whole-brain functional imaging at cellular resolution (Ahrens et al., 2013; Panier et al., 2013), and imaging sizeable volumes of the mammalian brain (Holekamp et al., 2008). Moreover, the relatively high volumetric speed of this technique can be advantageous when imaging large, fixed specimens,

Table 1. 3D Fluorescence Microscopy Methods

	Light Sheet	Light Field	Two-Photon Point Scanning	Two-Photon Random Access
Speed	Moderate for volumes	High for volumes	Low for volumes	Low for volumes
	High for single planes		Moderate for single planes	Moderate for single planes
				Very high for a limited number of points distributed in a volume
Spatial resolution	High for Gaussian beams	Moderate	High	High
	Very high for multiview imaging or Bessel beams			
Signal/noise ratio	High for one-photon excitation	High	Low	Moderate for parallelized point detection
	Moderate for two-photon excitation			Low for sequential point detection
Depth penetration	High for two-photon excitation	Moderate (unsuited for two-photon excitation)	High	High
	Moderate for one-photon excitation		Very high with adaptive optics	
Geometric accessibility	High for small specimens	High	High	High
	Low for large specimens (most implementations require access from two orthogonal directions)			
Cost	Low for basic implementations	Low	High	High
	Moderate to high for advanced (e.g., multiarm or two-photon) implementations			
Key applications	Imaging small or fairly transparent specimens (such as embryos)	Instantaneous volume acquisition	Volumetric imaging deep inside nontransparent tissues	Imaging of sparsely labeled specimens at very high speed
	High-resolution volumetric imaging	Short-term volumetric imaging at high speed		
	Long-term volumetric imaging			

e.g., to facilitate rapid imaging of entire fixed mammalian brains (Dodt et al., 2007; Susaki et al., 2014; Tomer et al., 2014).

Imaging techniques each have their strengths and weaknesses. In the case of light-sheet microscopy, geometric access can be an obstacle. Since the most commonly used implementations of this technique require at least two objectives—one for illumination and one for detection—it is challenging to apply this technique to larger brains in intact animals. Although implementations with access to large, planar geometries exist, as discussed later (Holekamp et al., 2008), using microscopes with a single objective is typically more straightforward and leaves more space for other apparatus around the brain. Single-objective microscopy techniques include, e.g., two-photon microscopy and light-field microscopy. Some of the advantages and disadvantages of these different microscopy methods are discussed in Table 1.

In this Primer, we provide a brief introduction to the basic principles of light-sheet microscopy, discuss recent technical advances that are of particular interest to the neuroscience community, and provide examples of how this imaging technique enables new types of experiments that aim to advance our understanding of nervous system development and function. These light-sheet microscopy experiments frequently produce data sets of substantial size and complexity, typically at scales that are largely unprecedented in light microscopy. Therefore, we also discuss the data analysis challenges in developmental and functional light-sheet microscopy experiments and show how recent advances in computational image analysis can help convert light-sheet image data sets into biological insights.

Light-Sheet Microscopy

Conventional fluorescence light microscopes typically use the same objective for specimen illumination and fluorescence detection. This approach couples both processes and constrains the options for introducing spatial specificity in the illumination process. In contrast, light-sheet microscopy is based on the principle of decoupling illumination and detection by sending a thin "sheet" of laser light into the sample from the side using a dedicated objective. This concept originates from the "Ultramicroscope" developed by Siedentopf and Zsigmondy (1903) more than 100 years ago. Through the pioneering work by Voie et al. (1993) in the 1990s, this concept has been further developed into modern laser light-sheet fluorescence microscopy and introduced to biological imaging. Another decade later, Fuchs et al. (2002) and Huisken et al. (2004) beautifully applied the method for the first time to live imaging in microbial oceanography and developmental biology, respectively.

This light sheet is typically produced by focusing a millimeter-sized Gaussian beam with a cylindrical lens (Fuchs et al., 2002; Huisken et al., 2004; Voie et al., 1993) (Figure 1E) or by rapidly

scanning a micrometer-thin laser beam across the field of view (Keller et al., 2008) (Figure 1F). Fluorescence emitted by the illuminated sample section is subsequently detected with a separate camera-based wide-field arrangement. Through the use of two independent optical systems for sample illumination and fluorescence detection, the axis of incident laser light can be set at a right angle relative to the axis of fluorescence detection. In this configuration, the thin volume section of the sample that is illuminated by laser light can be aligned perfectly with the thin focal volume imaged by the microscope's detection arm. By moving the light sheet and detection objective relative to the specimen in small steps (or by just moving the specimen itself), one image after the other is recorded in rapid succession to obtain a 3D image stack of the entire specimen volume.

Many different practical implementations and extensions of the conceptually old idea of light-sheet microscopy (Siedentopf and Zsigmondy, 1903) have been developed to date (Keller, 2013; Keller and Dodt, 2012; Mertz, 2011; Santi, 2011; Weber and Huisken, 2011; Winter and Shroff, 2014). In particular, over the past few years, new designs have emerged that are well suited to address imaging challenges encountered in developmental and systems neuroscience. Recent key performance advances in light-sheet microscopy relate to improvements in imaging speed, spatial resolution, deep-tissue imaging, and multiview imaging of large biological specimens. Advances in imaging speed, up to rates of hundreds of millions of volume elements per second, have enabled the design of light-sheet microscopes suitable for whole-brain functional imaging experiments at volumetric imaging rates that match the time scales of genetically encoded calcium indicators (Ahrens et al., 2013; Panier et al., 2013). Breakthroughs in spatial resolution—enabling up to 10-fold improvement in axial resolution and, therefore, isotropic spatial resolution on the order of 300 nm—have been demonstrated for single cells (Majoul et al., 2013; Planchon et al., 2011) and even small multicellular organisms (Gao et al., 2012; Wu et al., 2013). Advances in deep-tissue imaging and physical coverage of large biological specimens have been achieved through the introduction of multiphoton excitation in light-sheet microscopy (Truong et al., 2011) and through the implementation of light-sheet microscopes capable of imaging multiple complementary views of the sample simultaneously (Krzic et al., 2012; Schmid et al., 2013; Tomer et al., 2012). A comparison of some of the most commonly used imaging strategies in light-sheet microscopy is presented in Table 2.

Developmental Imaging of the Nervous System Using Light-Sheet Microscopy

Over the past few years, several types of light-sheet microscopes and light-sheet based imaging assays have been developed to investigate nervous system structure as well as the dynamic processes underlying its development (Figure 2; Figure 3; Figure 4). Using live imaging approaches, light-sheet microscopes have been used to image dynamic processes over a wide range of spatial and temporal scales, from fast structural changes in the architecture of gap junctions (Majoul et al., 2013) and filopodial dynamics during axonal morphogenesis (Tomer et al., 2012) to whole-embryo imaging of *C. elegans* and *D. melanogaster* nervous system development with subcellular resolution (Tomer et al., 2012; Wu et al., 2011, 2013). In parallel to these efforts in the domain of developmental live imaging, several other groups developed strategies for structural whole-brain imaging, with a particular focus on rapid imaging of fixed and cleared mammalian brains (Dodt et al., 2007; Susaki et al., 2014; Tomer et al., 2014). These light-sheet-based imaging assays provided for the first time comprehensive reconstructions of cell morphologies in intact, centimeter-sized brains with cellular resolution. Altogether, this spectrum of imaging experiments covers spatial scales from a few hundred nanometers to several millimeters and temporal scales from a few seconds to several days. These experimental demonstrations serve as helpful examples for illustrating the capabilities of light-sheet microscopy in developmental neuroscience applications and will be briefly examined in the following sections.

Improving Spatial Resolution with Bessel Beams

The properties of Bessel beams (Fahrbach et al., 2010; Planchon et al., 2011) can be exploited to address a fundamental limitation in resolution encountered in "conventional" light-sheet microscopes relying on Gaussian beams. When using Gaussian beams, the light-sheet microscope typically suffers from anisotropic resolution, since the microscope's lateral resolution, which depends on the numerical aperture of the detection objective and is typically on the order of a few hundred nanometers, is usually significantly better than the microscope's axial resolution. The latter, which is typically on the order of a few micrometers (and proportional to the square root of the size of the field of view), depends on the numerical aperture of the detection objective as well, but it is also directly influenced by the thickness of the laser beam used for sample illumination. As the name suggests, Bessel beam plane illumination microscopy (Planchon et al., 2011) uses a scanned Bessel beam to illuminate the sample in a thin volume section. This Bessel beam consists of a system of concentric rings around a central peak, which can be made to be significantly thinner than a Gaussian beam for a given field of view. In order to achieve good axial resolution, the microscope is operated so that only fluorescence generated in response to illumination with the thin, central peak contributes to the final image. For this purpose, a structured illumination mode is typically used to remove signal contribution by the concentric ring system. Overall, this approach can provide significantly better axial resolution than Gaussian beam light-sheet microscopy for the same field-of-view size, but it also generates a significantly higher energy load on the sample arising from the Bessel beam's concentric ring system. For example, in imaging experiments with *Drosophila* egg chambers, a 2-fold improvement in axial resolution using Bessel beams was accompanied by an increase in energy load on the sample by a factor of six (Fahrbach and Rohrbach, 2012).

Using Bessel beam plane illumination microscopy with near-isotropic resolution in the 300 nm range, Majoul et al. (2013) imaged the remodeling of proteins and lipids within gap junction plaques in response to bacterial AB5 toxin exposure. They achieved volumetric imaging speeds of one volume per 20 s and observed rapid rearrangements in connexin channels that lead to increased connexin packing and lipid reorganization. Furthermore, the authors performed a side-by-side comparison of their method to spinning-disk confocal microscopy,

Table 2. Tradeoffs for Commonly Used Imaging Strategies in Light-Sheet Microscopy

Static versus Scanned Light Sheets		
	Light Sheet Generated by Cylindrical Lens (SPIM)	Light Sheet Generated by Laser Scanning (DSLM)
Speed	High (limited by camera)	High (limited by camera)
Spatial resolution	High (isotropic spatial resolution achievable for transparent specimens through multiview imaging and image deconvolution; Wu et al., 2013)	High (isotropic spatial resolution achievable through multiview imaging and image deconvolution or Bessel beams; Gao et al., 2012; Planchon et al., 2011)
Depth penetration	Moderate (unsuited for two-photon excitation across a large field of view and incompatible with Bessel beams)	High (through use of efficient two-photon excitation and/or Bessel beams; Fahrbach and Rohrbach, 2012; Truong et al., 2011)
Peak power and photobleaching	Low (simultaneous signal collection from the entire field of view)	Moderate (same average power as SPIM but higher peak laser power density due to 1D scanning of field of view)
Imaging artifacts	High (prone to striping artifacts due to coherent illumination [Rohrbach, 2009]; mitigation of striping possible through light sheet pivoting [Huisken and Stainier, 2007]; nonuniform laser power density across field of view)	Moderate (less prone to striping artifacts due to incoherent illumination [Rohrbach, 2009]; mitigation of striping possible through Bessel beams [Rohrbach, 2009]; uniform laser power density across field of view [Keller et al., 2008])
Two-photon excitation capability	Low (relatively inefficient, low speed, and small field of view owing to low power density)	High (high efficiency owing to high power density; Truong et al., 2011)
Structured illumination capability	Moderate (requires mask; reduced image quality, slow and fixed pattern frequency when implemented mechanically)	High (precise, fast, efficient, and digitally adjustable structured illumination through intensity modulation of the illuminating laser beam; Keller et al., 2010; Mertz and Kim, 2010)
Confocal imaging capability	None (intrinsically incompatible due to use of simultaneous whole-plane illumination)	High (implementation through use of rolling shutter in sCMOS cameras)
Beam shaping control	Low (limited control over beam shaping due to simultaneous formation of an illumination profile covering the entire plane)	High (implementation of Bessel and Airy beams, easy and efficient field-of-view control, well suited to adaptive optics through use of laser scanning)
Key applications	Imaging of small/transparent samples or single planes at very high speeds	High-speed, high-resolution imaging of larger samples High-contrast one- and two-photon imaging of light-scattering samples
Gaussian versus Bessel Beams		
	Gaussian Beam	Bessel Beam
Spatial resolution	High (multiview imaging required to achieve isotropic spatial resolution in sufficiently transparent specimens; Wu et al., 2013)	High (thin central peak of Bessel beam enables resolution enhancement when combined with confocal line scanning, two-photon excitation or structured illumination; Fahrbach and Rohrbach, 2012; Planchon et al., 2011)
Depth penetration	High for two-photon excitation Moderate for one-photon excitation	High (improved propagation stability compared to Gaussian beam at visible wavelengths [Fahrbach and Rohrbach, 2012] but two-photon excitation required for optimal depth penetration)
Peak power and photobleaching	Low (low peak power density and efficient use of the sample's photon budget)	Moderate (high peak power density and significant increase in rates of photobleaching and -toxicity in all use cases, i.e., two-photon excitation and structured illumination [Planchon et al., 2011], as well as confocal line scanning [Fahrbach and Rohrbach, 2012])
Imaging artifacts	Moderate (striping artifacts arising from light scattering and absorption)	Low (reduction in striping artifacts due to improved propagation stability; Fahrbach and Rohrbach, 2012)
Illumination/detection efficiency	High (minimal laser light losses, no selectivity in detection process required)	Moderate (laser light losses as a result of beam shaping with spatial light modulators or axicons combined with masks/apertures; contribution of side lobes in the Bessel beam's profile to final image formation must be actively suppressed)
Key applications	Long-term, high-speed in vivo imaging under physiological conditions	High-resolution imaging

(*Continued on next page*)

Table 2. *Continued*

One-Photon versus Two-Photon Excitation		
	One-Photon Excitation	Two-Photon Excitation
Speed	High (higher signal rates in one-photon excitation allow for lower exposure times and higher frame rates)	Moderate
Spatial resolution	High	High (potential of higher lateral and axial resolution through lower background contribution [Truong et al., 2011], but difficult to exploit in practice because of lower signal-to-noise ratio)
Signal-to-noise ratio	High	Moderate
Depth penetration	Moderate	High (improved depth penetration at infrared illumination wavelengths)
Suitability for behavioral assays and optogenetics	Moderate (visible wavelengths can cause responses of the visual system, but instrument designs exist that are suitable for vision and behavior in zebrafish [Vladimirov et al., 2014]; difficult to achieve spectral separation of indicator and effector channels)	High
Suitability for multicolor imaging	High (easy and versatile imaging of many color channels simultaneously, wide selection of dyes and fluorescent proteins)	Moderate (limited selection of dyes and fluorescent proteins that can be used efficiently with two-photon excitation; simultaneous imaging of multiple color channels possible with advanced instrument designs; Mahou et al., 2014)
Cost	Low	High (pulsed infrared laser required)
Key applications	High-speed imaging	Imaging deep inside nontransparent biological tissues
	General-purpose imaging with high signal-to-noise ratio	
	General-purpose multicolor imaging	

SPIM, selective plane illumination microscopy; DSLM, digital scanned laser light sheet microscopy.

demonstrating a substantial resolution improvement and the general importance of their light-sheet-based imaging strategy in enabling these detailed observations of fine structural dynamics.

Improving Spatial Resolution by Alternating between Illumination and Detection

Following a different light sheet-based imaging strategy, Wu et al. developed inverted selective plane illumination microscopy (iSPIM) (Wu et al., 2011) and dual-view iSPIM (diSPIM) (Wu et al., 2013) to image neural wiring during *C. elegans* brain development (Figures 2A and 2B). The basic iSPIM design takes advantage of existing, commercially available hardware as a microscope base and extends this system with a light-sheet illumination module and camera-based detection arm. In contrast to many other light-sheet microscope designs, the iSPIM geometrical arrangement of these two arms at a 45° angle relative to the microscope base supports the use of a conventional coverslip/slide-based sample preparation. This strategy of light-sheet imaging under a 45° angle in iSPIM has been utilized also in the Bessel beam plane illumination microscope discussed earlier (Planchon et al., 2011) and in objective-coupled planar illumination microscopy (OCPI) for functional imaging of mammalian neural tissues (Holekamp et al., 2008). diSPIM takes this design one step further by dynamically alternating illumination and detection between the microscope's two objectives. Thereby, two complementary views of the sample are recorded in rapid succession, providing alternating orientations of the microscope's point spread function. If the specimen is sufficiently small and transparent to ensure comparable physical coverage in both views, the acquired image data can subsequently be computationally fused to enhance spatial resolution down to an isotropic resolution of 330 nm. By applying iSPIM and diSPIM to neurodevelopmental imaging in *C. elegans*, Wu and colleagues (Wu et al., 2011, 2013) followed neurite outgrowth and neural wiring at speeds of up to 30 volumes per minute. A systematic comparison of diSPIM to spinning-disk microscopy in the context of nuclei-labeled *C. elegans* embryos revealed improvements in axial resolution (2-fold) and volumetric imaging speed (10-fold), as well as reduced photobleaching (7.6-fold). A quantitative analysis of neurite development in AIY interneurons with diSPIM showed that AIY extend projections at different rates during the development of different zones. Since these zones are also functionally distinct, Wu et al. (2013) suggest that there may be a link between synaptic polarity and the axon growth dynamics measured in their study.

Rapidly Covering Larger Volumes by Simultaneous Multiview Imaging

In order to image nervous system development in an entire *Drosophila* embryo with subcellular resolution, Tomer et al.

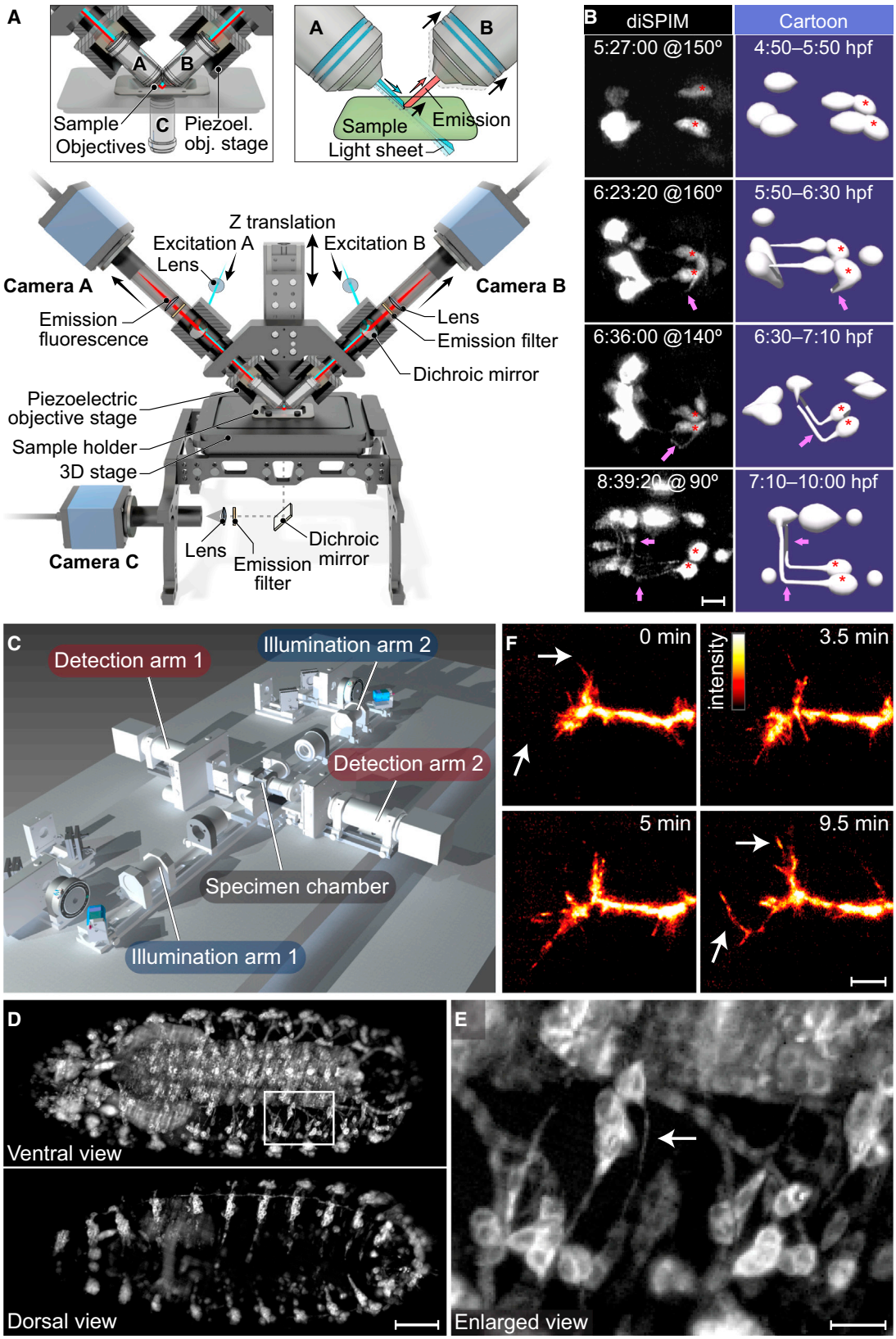

(legend on next page)

(2012) developed simultaneous multiview (SiMView) light-sheet microscopy (Figure 2C). This microscope design effectively addresses the fundamental challenges associated with the imaging of fast dynamic processes in large, nontransparent specimens. In light microscopy, typically only a fraction of a large specimen's volume is visible from one view angle, owing to the limited penetration of biological tissues at physiological wavelengths. For example, when using a conventional light-sheet microscope with a single illumination arm and a single detection arm oriented at a right angle to the illumination axis, only about a quarter of a *Drosophila* embryo's volume is visible. Light scattering and light absorption preclude access to the remaining parts, unless the specimen is rotated to acquire multiple views. Mechanical rotation, however, is time consuming and compromises the observation of fast dynamic processes at the whole-embryo scale. SiMView microscopy (Tomer et al., 2012) and a similar method named multiview SPIM (MuVi-SPIM) (Krzic et al., 2012) overcome this problem by pointing four objectives at the sample (following the pattern of a cross) and using, simultaneously, two of these objectives for sample illumination and two objectives for fluorescence detection. Since the two light sheets and the two detection focal planes can be positioned in a coplanar arrangement, this approach makes it possible to record four complementary views of the sample simultaneously (Figures 2D–2F). It is straightforward to fully exploit this capability in two-photon acquisition mode, where fluorescence excitation by each of the two light sheets is spatially confined to the respective focal volume (Tomer et al., 2012; Truong et al., 2011). However, when using one-photon excitation, which leads to fluorescence generation along the entire length of the light sheet, sample illumination with the two light sheets usually needs to be performed sequentially to produce optimal results. By stitching the resulting images together computationally, the contribution of each light sheet to the final image is restricted to the respective half of the field of view the light sheet is centered on and, thus, a possible contribution of background fluorescence of the rapidly widening light sheets to the respective other half of the field of view is prevented. High image contrast can alternatively also be restored, at least partially, for simultaneous bidirectional illumination by using confocal slit detection (Baumgart and Kubitscheck, 2012).

The unique views provided by each of the four possible combinations of illumination and detection objectives are registered in space and fused to produce a single image stack with close-to-complete physical coverage of the sample. Using fast scientific complementary metal-oxide semiconductor (sCMOS) cameras for detection, early implementations of this method provided imaging speeds on the order of 175 million voxels per second. It should be noted that this use of multiview imaging is conceptually different from the acquisition of complementary views, e.g., in the diSPIM implementation by Wu et al. (2013), as both techniques address different limitations in light microscopy. Whereas SiMView and MuVi-SPIM acquire multiple views of a nontransparent sample to increase physical coverage (with fixed orientation of the point spread function across all views), diSPIM acquires multiple views of a transparent sample with different orientations of the point spread function to improve axial resolution (but without changing physical coverage).

By applying SiMView to live imaging of *Drosophila* embryos, Tomer et al. (2012) followed nervous system development throughout embryogenesis in 30 s intervals and with subcellular resolution. The whole-embryo imaging assay presented in this study thus offers a global view of neurodevelopmental processes and, at the same time, reveals detailed filopodial dynamics during axonal morphogenesis. Using SiMView developmental imaging of *Ftz-ng-Gal4* lines with sparse expression in the CNS, Tomer et al. (2012) showed that zones of filopodial extension and exploration are retained in regions proximal from the growth cones over long periods of time. Further advances of the imaging technique led to improvements in volumetric imaging rates by more than one order of magnitude,

Figure 2. System-Level Imaging of Nervous System Development in *C. elegans* and *Drosophila*

(A) Schematics of a diSPIM light-sheet microscopy setup. Two water-immersion objectives (A/B) are mounted orthogonally and, together with the other optical elements in the respective optical arm, produce thin laser light sheets at the location of the sample. Fluorescence light collection occurs via the same objectives. Light collected by objective A is imaged onto camera A, and the same applies to objective B and camera B. Although excitation (blue) and detection (red) are shown occurring simultaneously along both light paths in the lower panel, volumetric imaging actually occurs sequentially, as shown in the upper right panel. The sample and the objective used for illumination are held stationary during image acquisition. At the same time, the light sheet is scanned across the sample volume using galvanometer scanners, while a piezo moves the objective used for detection in sync with the light sheet so that excitation and detection planes are coincident. Objective C and camera C under the sample translation stage aid in finding or screening samples for subsequent imaging. Piezoel. obj., piezoelectric objective.

(B) Spatiotemporal dissection of AIY neurite outgrowth. The images at the left show diSPIM maximum intensity projections at the indicated time points (provided in hours:minutes:seconds postfertilization) and for the indicated rotation angles. Red stars and pink arrows indicate the position of AIY cell bodies and neurites, respectively. A cartoon of the developmental process is shown at the right. hpf, hours postfertilization.

(C) Optical implementation of the SiMView light-sheet microscopy platform for SiMView in vivo imaging of large biological specimens. The specimen is attached to a thin cylindrical specimen holder and is optically accessible from all sides. Fluorescence excitation is performed in a micrometer-thin volume by two overlapping scanned light sheets that are focused into the specimen chamber by two opposite long-working-distance illumination objectives. Two opposite detection objectives collect the fluorescence light emitted by the specimen. Each of the four combinations of light sheets and detection objectives provides a different view of the specimen.

(D) SiMView imaging of *Drosophila* neural development. The images show maximum-intensity projections of *Drosophila* embryonic nervous system development recorded in an elavC155-GAL4;UAS-mCD8::GFP transgenic embryo with SiMView microscopy. Dorsal and ventral views of the same embryo were captured simultaneously by the two cameras in the SiMView microscope. Imaging was performed at 30 s intervals over the period of 9.5–15.3 hr after egg laying, producing a 4-terabyte image data set comprising ~700 time points.

(E) Enlarged view of the area highlighted in (D). The arrow points to an axon.

(F) The images show maximum-intensity projections of axonal morphogenesis in a Ftz-ng-GAL4;10xUAS-IVS-myr::GFP transgenic embryo recorded with SiMView microscopy. Only a 0.3% subregion of the total imaged volume is shown to better illustrate the spatial resolution achieved in these system-level recordings. Arrows highlight regions of filopodial dynamics.

Scale bars, (B and F) 5 μm; (D) 50 μm; (E) 10 μm.

(A) and (B) were adapted with permission from Wu et al. (2013). (C) through (F) were adapted from Tomer et al. (2012).

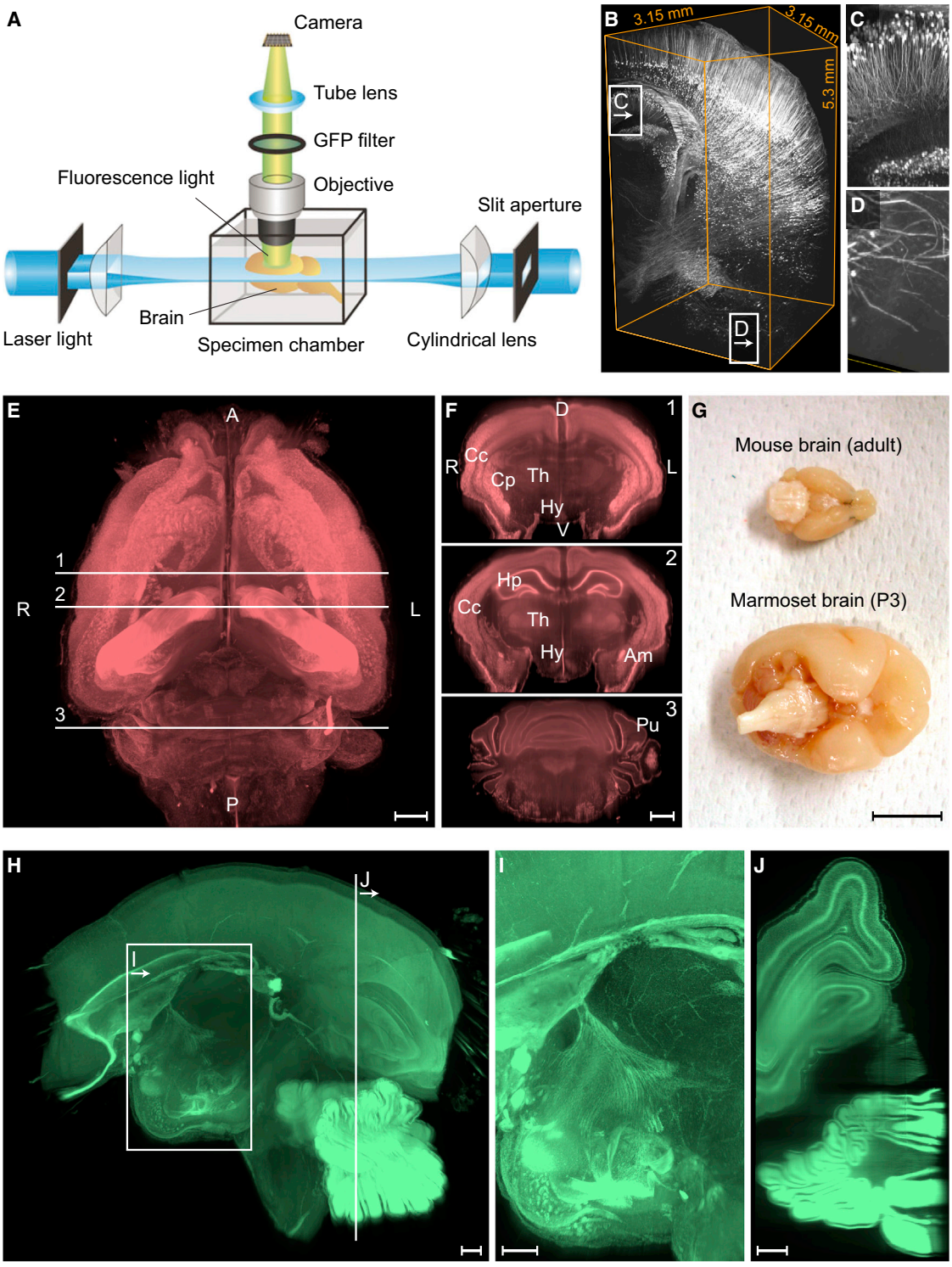

Figure 3. Imaging Chemically Cleared Mouse Brains

(A) Ultramicroscopy for imaging entire cleared mouse brains. The sample is illuminated from two sides with laser light sheets. Fluorescence is emitted only from the thin optical section illuminated with these sheets, collected by the detection objective and imaged onto a camera.

(B) High-resolution imaging of a clarified brain using CLARITY-optimized light-sheet microscopy. The image shows a 3.15 mm × 3.15 mm × 5.3 mm volume acquired from an intact clarified Thy1-eYFP mouse brain with a 25× detection objective. The brain was perfused with 0.5% (wt/vol) acrylamide monomer solution. The complete data set was acquired in ~1.5 hr.

(C and D) Magnified views of the regions in (B) highlighted by white boxes.

(legend continued on next page)

providing a temporal resolution on the order of 1 s for even larger sample volumes (Ahrens et al., 2013).

These new imaging capabilities also led to new challenges in the computational analysis of the resulting image data. SiMView image data sets provide highly complex, dynamic information of cellular and nuclear morphologies throughout the embryo, comprising high-resolution image data of up to 10 terabytes per experiment. The need for efficient strategies to analyze such data sets triggered the development of automated computational methods for the fast and accurate reconstruction of cell lineage data. The computational method developed by Amat et al. (2014), which is discussed in more detail in the section "Analysis of Large-Scale Developmental and Functional Image Data," enabled automated tracking of cell identities in large-scale fluorescence microscopy data sets and was used to perform the first cell lineage reconstruction of early *Drosophila* nervous system development.

Light-Sheet Imaging of Entire Cleared Mammalian Brains

The high imaging speed and low photodamage of light-sheet microscopy is useful not only for noninvasive observation of dynamic processes in living specimens but also for rapid volumetric imaging of exceptionally large fixed specimens (Figure 3A). The development of chemical clearing methods (Chung et al., 2013; Dodt et al., 2007; Hama et al., 2011; Susaki et al., 2014; Tomer et al., 2014) and their integration with light-sheet microscopes designed for imaging of centimeter-sized specimens have made it possible to perform structural whole-brain imaging even for fairly large, mammalian brains (Dodt et al., 2007; Susaki et al., 2014) (Figure 3). By integrating light-sheet illumination modules in modified commercial macroscopes, several labs demonstrated rapid optical sectioning of entire mouse brains. To clear the mouse brains, Dodt et al. (2007) used a mixture of benzyl alcohol and benzyl benzoate, whose refractive index is matched to that of the fixed tissue. This chemical clearing technique reduces light scattering, greatly increasing imaging depth relative to conventional fixation methods. Using this approach, they were able to image fixed brains with single-cell resolution and perform reconstructions of dendritic trees and spines in populations of CA1 neurons in isolated hippocampi. Susaki et al. (2014) developed a class of reagents, referred to as CUBIC (clear, unobstructed brain imaging cocktails and computational analysis), which combine urea- and aminoalcohol-based treatments to perform light-sheet based imaging of mouse brains (Figures 3E and 3F) and even small primate brains at single-cell resolution (Figures 3G–3J). The CUBIC treatment turned out to be particularly well suited for use with fluorescent proteins. Susaki et al. (2014) demonstrated multi-color imaging with various types of fluorescent proteins and show that subcellular structures, including axons and dendritic spines, are well-preserved in the CUBIC-cleared specimens. Finally, Tomer et al. (2014) described a light-sheet-based approach to imaging CLARITY-cleared mouse brains. CLARITY treatment achieves lipid removal in a stable hydrophilic environment through electrophoresis (Chung et al., 2013), generating cleared volumes that can be treated with immunohistochemistry and in situ hybridization multiple times in succession, allowing for comprehensive anatomical analysis of the tissue. By implementing a light-sheet microscope for use with CLARITY-optimized detection objectives, Tomer et al. (2014) developed a rapid imaging strategy for entire mouse brains based on optical tiling of the fairly large specimen volume for high-resolution imaging at the whole-brain level (Figures 3B–3D).

Functional Imaging of the Nervous System Using Light-Sheet Microscopy

Advances in chemistry and protein engineering enabled optical measurement of neural activity through, for example, voltage indicators (Cao et al., 2013; Kralj et al., 2011; Siegel and Isacoff, 1997) and calcium indicators (Chen et al., 2013; Palmer and Tsien, 2006). Calcium imaging has been widely used as an indirect measure of neuronal spiking activity, and algorithms exist that attempt to extract spike trains from calcium data (Greenberg et al., 2008; Holekamp et al., 2008; Sasaki et al., 2008; Vogelstein et al., 2010; Yaksi and Friedrich, 2006). Electrical recordings—in particular, whole-cell recordings—are still considered the gold standard measurement of neuronal activity, but optical imaging has its advantages. Imaging neural activity is generally less invasive than inserting electrodes and, in many cases, can gather data from larger numbers of neurons. Notably, optical methods capture not only neural activity but also anatomy, providing information about neuron locations and morphology. In combination with colabeling of genetically defined cell types (Madisen et al., 2010), this can be particularly powerful—cell identity and cell activity can be simultaneously assessed. Wide-field, confocal, and two-photon microscopy have been applied extensively to the study of population activity in many animal species, with each imaging technique having its own strengths and applications, as detailed earlier. Light-sheet imaging excels at system-level imaging of small vertebrate and invertebrate brains, but it can also be useful for brain slices and areas of larger vertebrate brains.

In an early adoption of light-sheet microscopy in neuroscience, responses in the mouse vomeronasal organ (VNO) were assessed using OCPI (Holekamp et al., 2008) (Figures 4A–4E). To keep the light sheet exactly in the focal plane of the objective

(E) Whole-brain imaging of various fluorescent proteins with CUBIC. The image shows a rendering of a light-sheet fluorescence microscopy data set of an R26-pCAG-nuc-3 × mKate2 brain from a 5-week-old mouse (ventral view). A, anterior; P, posterior; R, right; L, left.
(F) Coronal sections of the image data at positions 1–3 indicated in (E). D, dorsal; V, ventral; R, right; L, left; Cc, cerebral cortex; Cp, caudoputamen; Th, thalamus; Hy, hypothalamus; Hp, hippocampus; Am, amygdala; Pu, Purkinje cell layer.
(G) Application of CUBIC to a primate brain. The image shows an adult mouse brain next to a postnatal day 3 (P3) marmoset brain.
(H–J) Rendered images in (H) and (I) and an image of a coronal section in (J) of a nuclear-stained marmoset brain hemisphere acquired with light-sheet fluorescence microscopy. A magnified view of the boxed region in (H) is shown in (I). A coronal section at the position indicated in (H) is shown in (J). Anatomical structures such as vessels and layers of the cerebral cortex are visible.
Scale bars, (E, F, and H–J) 1 mm; (G) 1 cm.
(A) was adapted with permission from Dodt et al. (2007). (B) through (D) were adapted with permission from Tomer et al. (2014). (E) through (J) were adapted with permission from Susaki et al. (2014).

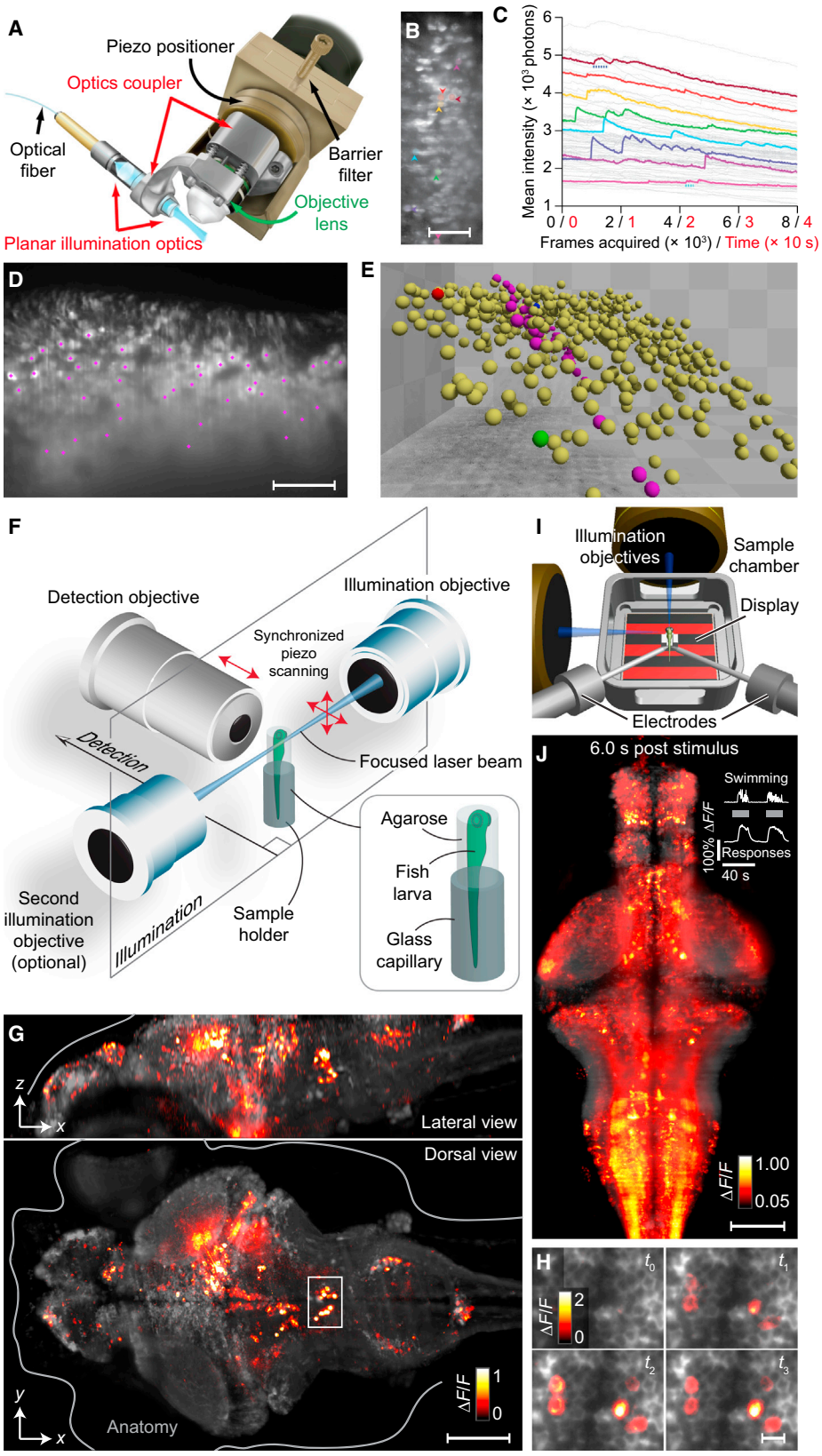

(legend on next page)

in this setup, the illumination optics are physically coupled to the objective (Figure 4A). This assembly can be rapidly moved along the axial direction of the detection objective with a piezo to perform volumetric imaging. Using this approach, Holekamp et al., 2008 were able to scan a volume of ~300 × 300 × 300 μm^3 at 2 s per volume. In this way, they could capture activity from about 1,000 neurons in the VNO and determine their tuning to a bank of chemical stimuli (Figures 4D and 4E). What this study achieved that could not easily be done before was to map a large volume of a sensory system; prior work in the VNO had demonstrated tuning to chemical stimuli (Holy et al., 2000) but only surveyed small regions of this brain area. In more recent work, Hammen et al. (2014) uncovered spatial relationships between glomeruli in the VNO that were tuned to related chemical stimuli, another example of a discovery that depends on imaging a large volume simultaneously.

In the larval zebrafish, light-sheet microscopy has been used to image from large fractions of the brain (Figures 4F–4J). This model organism is useful in both developmental biology and in neuroscience because it is largely transparent, especially when working with mutants such as *nacre* (Lister et al., 1999), which lack pigment in the skin. This means that microscopes have optical access to the entire brain, a fact that has been exploited in developmental studies for some time. The combination of the transparency and small size of this model organism, the availability of genetically encoded calcium indicators, and light-sheet microscopy allowed Ahrens et al. (2013) and Panier et al. (2013) to image activity in large numbers of neurons in the brains of zebrafish. In the former study, using volumetric light-sheet imaging at rates of about 1 Hz, nearly all neurons in the brain could be imaged, most (about 80%) at single-cell resolution (Figures 4F–4H). Brain-wide activity patterns were complex and multiplexed, and correlational methods uncovered some basic structure in neural activity. Light-sheet imaging has since been combined with fictive behavior (Vladimirov et al., 2014) in a setup where behavioral readout and visual stimulus delivery is combined with light-sheet microscopy (Figures 4I and 4J). To overcome the fact that typical light-sheet delivery also stimulates the eyes, two laser beams were used to scan the brain—one scanning the brain from the side, dynamically switching off whenever positioned over the eyes and the other scanning the remainder of the brain from the front, thus minimally affecting the visual system of the animal and allowing external visual stimulation to be delivered. This type of setup is able to generate whole-brain neuron resolution data during behavior, allowing for brain dynamics to be directly correlated to behavioral output and sensory input, thereby providing a platform for studying sensorimotor transformations and higher order brain function at the whole-brain level.

Brain activity imaging strategies depend crucially on the indicators used to report neural activity. Genetically encoded calcium indicators have rise times of a few tens of milliseconds and decay times of 1–2 s, making them suitable for two somewhat different purposes. To image fluctuations in neural activity, without resolution on single-spike time scales, imaging at speeds of a few Hertz is sufficient and can be accomplished for entire volumes with a light-sheet approach. If, on the other hand, one wants to make use of the relatively fast rise time and attempt to infer spike times, constraints on imaging speed are quite different—ideally, speeds above 50–100 Hz would be used to track the upswing of the calcium transients. For the spike timing regime, light sheets would typically have to be positioned in one plane in order to image at camera rates. Similarly, most voltage indicators (Cao et al., 2013; Kralj et al., 2011) operate in the fast regime, benefitting from imaging rates at or above

Figure 4. Functional Imaging of the Entire Zebrafish Brain and of Large Neuronal Populations in the Mouse Olfactory System

(A) Schematic of an OCPI light-sheet microscope. Laser light for fluorescence excitation is provided by an optical fiber and is shaped into a light sheet ~3–5 μm thick using two lenses. The light sheet is coplanar with the focal plane of the detection objective. By coupling the illumination optics to the objective lens, the alignment of the light sheet with the detection focal plane is maintained while scanning a sample volume using the piezoelectric positioner attached to the detection objective. Objective lens and illumination optics are designed for water immersion applications.

(B) Simultaneous high-speed calcium imaging of many VNO neurons located in a single optical plane. The image shows a single frame from a 40 s movie of VNO sensory neuron cell bodies imaged over a field of view of 1,004 × 140 pixels at 200 Hz. Fluorescence intensities of individual cells were subsequently analyzed, and a few illustrative cells are marked with colored arrows.

(C) Fluorescence intensity levels as a function of time for 88 cells in the area shown in (B). Cells marked with colored arrows in (B) are represented by traces of the same color in this plot. The gradual decline in fluorescence intensity is due to photobleaching; approximately 10^9 photons were collected from each cell during the acquisition period.

(D) Probing of responses to chemical stimuli of single VNO neurons by high-speed 3D calcium imaging. The image shows a single optical section of an intact VN epithelium labeled with Oregon Green BAPTA-1. Purple dots indicate the positions of single neurons.

(E) 3D rendering of the positions of all neurons in the 40-image stack. Cells highlighted in purple were located in the single section shown in (D). Each checker in the background is 100 μm on each side. The sensory surface of the tissue is at the top.

(F) Whole-brain, neuron-level light-sheet imaging in larval zebrafish in vivo. The zebrafish is embedded in agarose gel and positioned in front of the detection lens. The 4-μm-thick light sheet is generated by fast vertical scanning of a laser beam focused inside the fish by one or both illumination objectives oriented orthogonal to the detection objective. Fluorescence is recorded with a fast sCMOS camera. Volumetric imaging is performed by scanning the light sheet across the sample and moving the detection objective so that the light sheet always coincides with the focal plane.

(G) Whole-brain, neuron-level activity, reported by a genetically encoded calcium indicator in a week-old *Tg(elavl3:GCaMP5G)* fish. Panels show lateral and dorsal projections of changes in fluorescence intensity (ΔF/F) at one point in time. Whole-brain volumes were recorded in intervals of 1.39 s.

(H) Close-up of the boxed region in (G) showing changes in neural activity over time at single-cell resolution.

(I) Light-sheet imaging during fictive behavior. A larval zebrafish receives visual input from a display underneath, and intended motor output is recorded electrically from the tail. To avoid exposing the eyes to direct laser light, two laser beams are utilized, one scanning from the side but skipping over the eyes, and the second scanning the tissue between the eyes from the front. The detection objective, located above the chamber, is not shown.

(J) Whole-brain functional imaging during behavior in a *Tg(elavl3:GCaMP6s)* fish. The panels show dorsal maximum-intensity projections of ΔF/F over the entire volume during stimulus presentation (averaged over 24 trials), superimposed on the anatomical map (gray). Cells and neuropil distributed across the brain show activity during the optomotor response; the activity profile of one cell in the hindbrain is shown in the inset.

Scale bars, (B and D) 50 μm; (G and J) 100 μm; (H) 10 μm.

(A) through (D) were adapted with permission from Holekamp et al. (2008). (E) through (H) were adapted from Ahrens et al. (2013). (I) and (J) were adapted from Vladimirov et al. (2014).

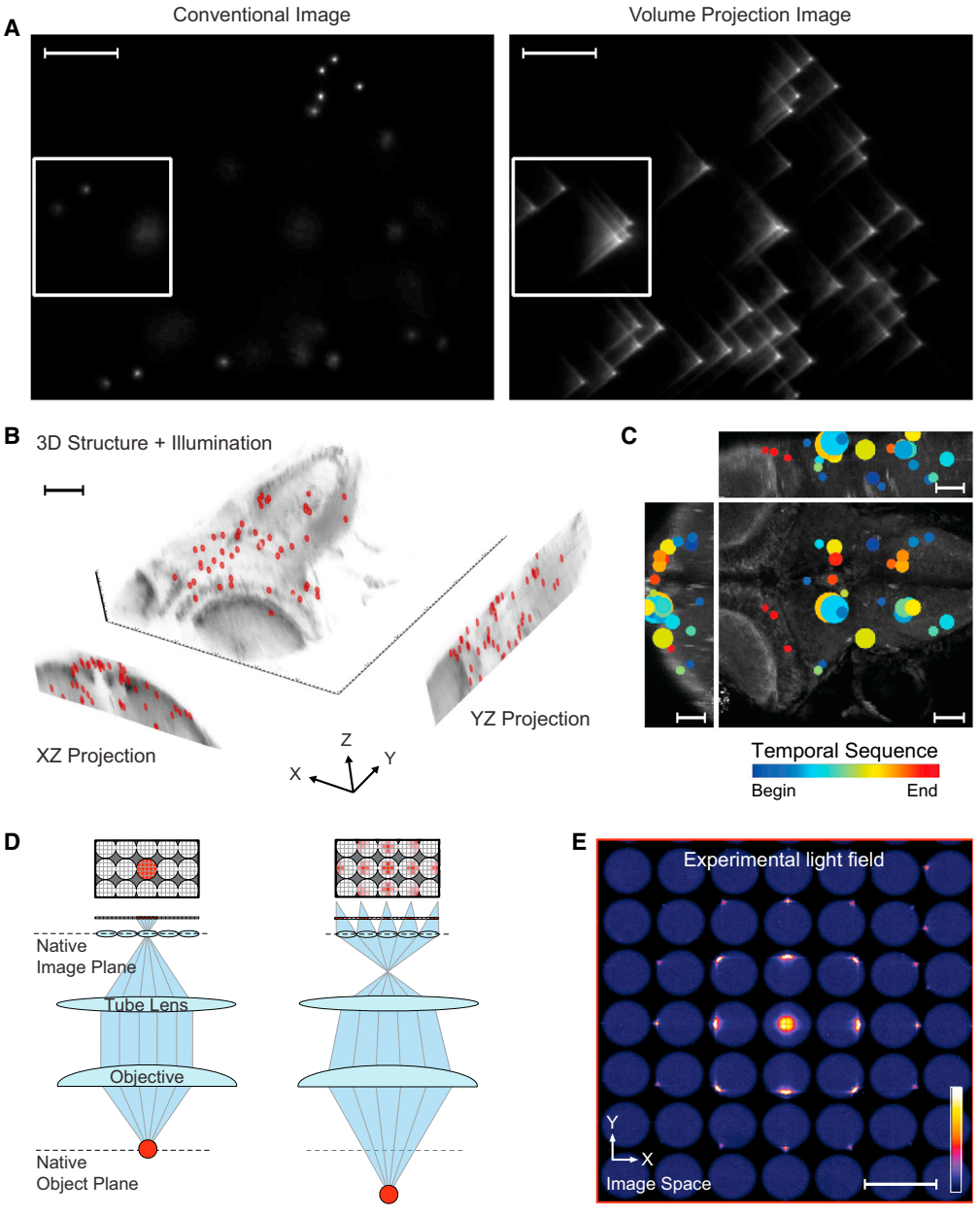

(legend on next page)

500 Hz and, thereby, from rapid light-sheet-based imaging of single planes. In the future, faster cameras will likely further increase the volumetric speeds of light-sheet imaging.

Alternatives to volumetric light-sheet imaging exist, which are capable of imaging at very high speeds, typically at the expense of spatial resolution or physical coverage (Table 1). A recent method for imaging at high speeds from a set of predetermined points in space (Quirin et al., 2014) is based on volume projection imaging, mediated by a phase mask in the detection pathway (Dowski and Cathey, 1995) and a spatial light modulator in the excitation pathway (Anselmi et al., 2011; Nikolenko et al., 2008) (Figures 5A–5C). This system can image at camera rates from many predetermined points in space using two-photon excitation. Other two-photon techniques utilize rapid 3D point scanning strategies to cover multiple points in space (Grewe et al., 2010; Katona et al., 2012) (Figure 1B).

Another promising volumetric imaging method is light-field microscopy (Figure 1D), in which wide-field illumination is combined with an optical detection system that allows for computational reconstruction of the 3D-imaged volume (Figures 5D–5G) (Levoy et al., 2006). This system makes use of an array of microlenses in the detection pathway combined with computational methods for reconstructing 3D volumes from 2D images. This method has been used by Grosenick et al. for volumetric imaging in zebrafish (Grosenick et al., 2009) and mammals (L. Grosenick, M. Broxton, and K. Deisseroth, personal communication) and by Prevedel et al. (2014) in entire *C. elegans*, including moving animals, and larval zebrafish (Figures 5F and 5G). High temporal imaging rates would make this method well suited for voltage imaging. Although the spatial resolution is not currently high enough to resolve single cells in the case of the whole zebrafish brain, single-cell resolution may be obtained in smaller volumes; in addition, future developments such as increases in the size of camera chips may help improve the spatial resolution of this technique.

Analysis of Large-Scale Developmental and Functional Image Data

Modern live imaging approaches reveal dynamic processes at the system level with unprecedented spatiotemporal resolution. The analysis of the resulting image data can be challenging with respect to both the complexity of the encoded information and the large size of the data sets. For example, using light-sheet microscopy, imaging the development of the *Drosophila* embryonic nervous system at the cellular level easily produces on the order of 10 terabytes of data per embryo, and even short-term functional imaging experiments still generate about 1 terabyte of image data per hour. Such data sets typically cannot be manually analyzed, and even just meaningful visualization of the image data can prove difficult. Quantitative analyses of nervous system development and function from large-scale image data thus require robust, automated computational approaches to extracting useful biological information. In this section, we provide examples of recently developed strategies that address these challenges.

Large-Scale Cell Lineage Reconstructions and Developmental Atlases

The choice and requirements of computational methods for automated image analysis depends, of course, on the biological problem of interest and the type of image data recorded. In the realm of developmental imaging, the most frequently encountered tasks include the reconstruction of cell positions, nuclei/cell boundaries, and cell tracks in fluorescently labeled specimens. Traditionally, methods used to address such tasks were designed for early developmental stages and relatively small 4D image data sets, comprising time-lapse information for up to a few thousand cells. However, the rapid advances in imaging capabilities in the past few years have triggered the development of new computational approaches to match these capabilities.

A framework for the fast, accurate extraction of cell positions, movements, and divisions from terabyte-sized fluorescence microscopy image data sets has recently been developed and evaluated for entire zebrafish, fruit fly, and mouse embryos expressing nuclear-localized fluorescent markers. This method by Amat et al. (2014) is capable of reconstructing cell lineages in advanced embryonic stages (Figures 6A and 6B) and, using a single computer workstation, extracts this information in less time than needed for the acquisition of the image data. This combination of speed and accuracy is achieved through three stages of analysis. In the first step, the size of the data set is reduced by

Figure 5. Instantaneous 3D Imaging with Wavefront Coding and Light-Field Microscopy

(A) Comparison between conventional wide-field (left) and volume (right) projection techniques. Each image is normalized to the respective peak signal.

(B) Simultaneous 3D in vivo imaging of neuronal activity at 49 targets in zebrafish at a rate of 30 volume projections per second. The targets are distributed throughout an acquisition volume of 284 × 270 × 114 μm^3.

(C) The 3D imaging approach shown in (B) uncovers temporal ordering of neural activity across the 49 targets. The temporal ordering is color coded, and the amplitude of signal modulation is coded by the size of the discs.

(D) Schematic of a light-field microscope. Left: A ray-optics schematic indicating the pattern of illumination generated by one point source. The gray grid delineates pixel locations, and the white circles depict the back aperture of the objective imaged onto the sensor by each lenslet. Red level indicates light intensity at the sensor. For a point source on the native object plane (red dot), all rays pass through a single lenslet. Right: A point source below the native object plane generates a more complicated intensity pattern involving many lenslets.

(E) A real light field recorded using a 60 × 1.4-NA oil objective and a 125 μm pitch f/20 microlens array of a 0.5 μm fluorescent bead placed 4 μm below the native object plane. Diffraction effects are present in the images formed behind each lenslet.

(F) Whole-animal Ca^{2+} imaging of *C. elegans* using light-field microscopy. Left: A wide-field image of the worm immobilized inside a microfluidic polydimethylsiloxane device. The head is at the bottom right. Right: Close-up of the brain region, with the maximum intensity projection of the xy plane as well as xz and yz cross-sections indicated by the dashed red lines.

(G) Maximum-intensity projections of a light field deconvolution volume (L. Grosenick, M. Broxton, and K. Deisseroth, personal communication) showing the brain of a zebrafish expressing GCaMP7a (Muto et al., 2013) reconstructed from a single 40 ms camera exposure during time-lapse imaging at 20 Hz. Dotted white lines show the location of the eyes. Fluorescence traces from four regions of interest are shown on the bottom right (timescale = 25 s).

Scale bars, (A and C) 50 μm; (B) 100 μm; (E) 125 μm; (F) 10 μm; (G) 200 μm.

(A) through (C) were adapted with permission from Quirin et al. (2014). (D) and (E) were adapted with permission from Broxton et al. (2013). (F) was adapted with permission from Prevedel et al. (2014).

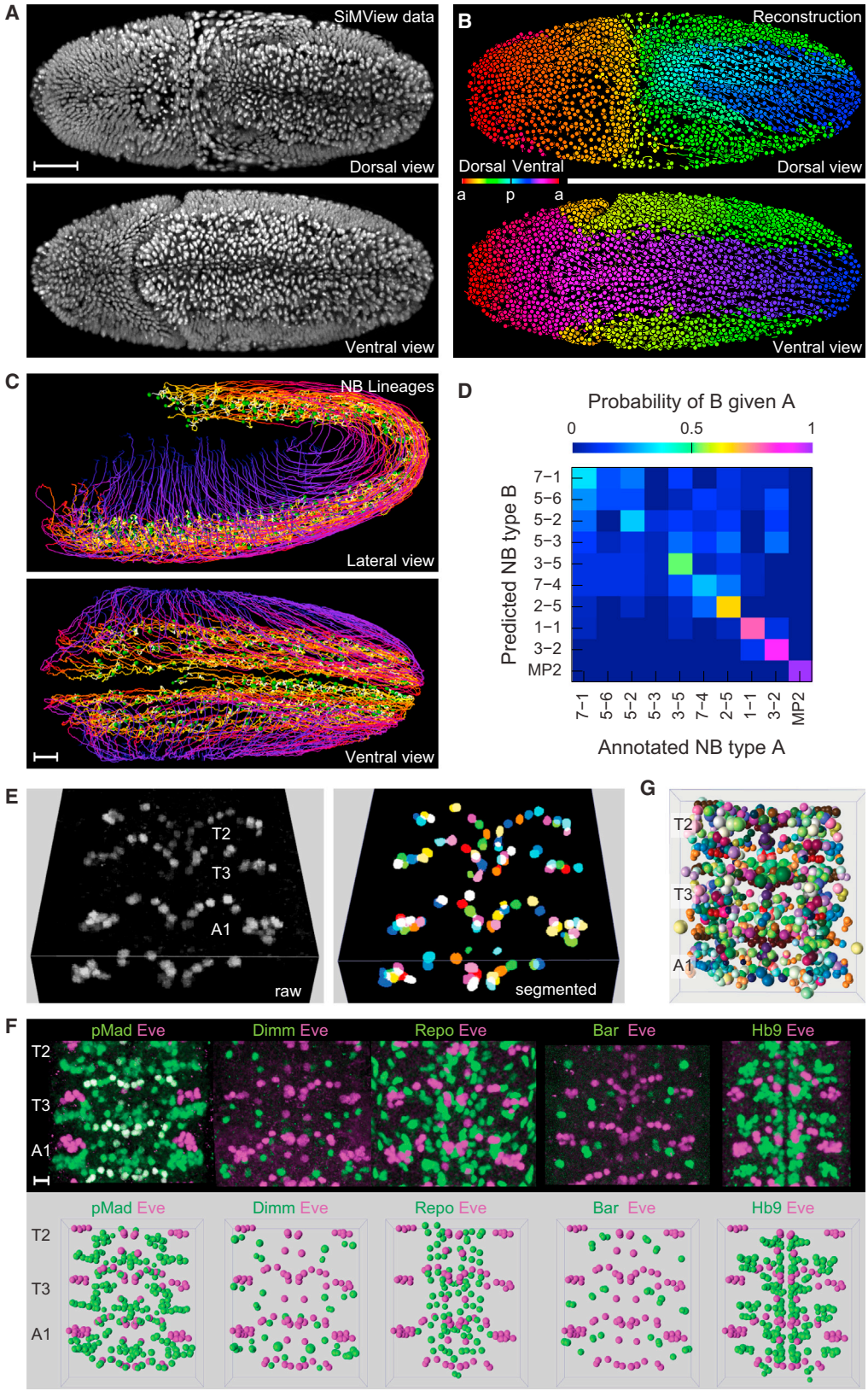

(legend on next page)

several orders of magnitude by grouping the image voxels into so-called supervoxels. Thereby, the framework can represent each cell nucleus with a small number of supervoxels (instead of thousands of voxels). In the second step, a simple shape model is fitted to the supervoxel data to group the supervoxels in space and time. The fit obtained for a given time point is also used to initialize the next time point, which allows the tasks of object segmentation and tracking to be performed simultaneously. Detailed morphological information is retrieved for each segmented nucleus by postprocessing the respective group of supervoxels. In the last step, local spatiotemporal windows are analyzed around each detected nucleus to identify and correct possible errors in the reconstruction.

Amat et al. (2014) applied their framework to the analysis of the *Drosophila* embryonic nervous system and performed a reconstruction of neuroblast cell lineages in the entire early ventral nerve cord (Figures 6C and 6D). The analysis of this system-level cell lineage reconstruction revealed that relative spatial arrangements of cells are almost perfectly preserved between ventral neurogenic regions in the blastoderm and the neuroblast array subsequently formed by neuroblast delamination. Moreover, Amat et al. found that about half of the S1 neuroblast types formed in the early *Drosophila* embryo exhibit characteristic cell behaviors already within the first 2 hr following the blastoderm stage, to an extent that the identities of these neuroblast types can be computationally predicted with fairly high accuracy solely from quantitative information on their movement and division patterns (Amat et al., 2014) (Figure 6D).

Increasingly complex data sets are generated not only in the domain of live imaging of nervous system development but also through large-scale imaging of the fixed nervous system. Such efforts introduce complementary computational challenges, e.g., the creation, integration, and comparison of static atlases of gene expression and cell-type-specific markers for the nervous system. To this end, Heckscher et al. (2014) recently introduced software that addresses the general problem of building an atlas of tissues that contain cell populations in stereotyped arrangements (Figures 6E–6G). By using the transcription factor Even-skipped as a reference marker, Heckscher et al. combined expression patterns from 75 Gal4 lines for the CNS of stage 16 *Drosophila* embryos. The 3D image stacks recorded from multiple specimens are first segmented and then annotated and registered using the reference marker. With this approach, Heckscher et al. built the eNeuro atlas, which contains eight transcription factors to mark the major CNS cell types as well as the new set of Gal4 lines. This atlas identifies more than 50% of all interneurons in the ventral CNS and serves as a further extendable resource for the community.

Large-Scale Functional Image Data Analysis

Functional imaging of large networks of neurons brings its own analytical challenges. The data sets are similarly large in size, and complexity here does not arise from phenomena such as the emergence of anatomical patterns but primarily from the interdependence of the activity of the many neurons across the CNS. One approach to understanding how the individual parts of this system—the neurons, synapses, molecular processes, etc.—interact to give rise to the function of the whole is to attempt to model the system in detail and run a simulation. Complementary, more directly data-driven approaches include dimensionality reduction, where the dynamics of large neuronal populations are described using fewer variables than the number of neurons, with the goal of capturing the degrees of freedom that are most important for the function of the brain, typically in a specific setting such as a task or stimulus condition (Briggman et al., 2005; Churchland et al., 2012; Freeman et al., 2014). Hybrid approaches include combinations of dimensionality reduction and modeling of network dynamics (Pfau et al., 2013; Yu et al., 2007).

One way in which neural function can be linked to external variables such as sensory input and behavior is through regression,

Figure 6. System-Level Reconstruction of Cell Lineages and Atlas Building for Embryonic Nervous System Development

(A and B) Automated cell lineaging in entire *Drosophila* embryos. (A) Maximum-intensity projections of SiMView image stacks of a nuclei-labeled stage 9 *Drosophila* embryo (see Supplementary Video 1 in Amat et al., 2014, for the complete data set). (B) Automated reconstruction of cell positions (spheres) and cell movements (lines, each indicating the respective cell movement over the past 5 min) from the SiMView recording shown in (A), using a color code that indicates blastoderm lineage origin (see Supplementary Video 2 in Amat et al., 2014, for the complete reconstruction). The color code was initialized in the first video frame using a color gradient from anterior to posterior. Different parts of the color spectrum were assigned to the dorsal and ventral sides while ensuring continuity in color space at the anterior and posterior ends of the embryo. The reconstruction comprises 501 time points (3–7 hr after egg laying, developmental stages 6–11). a, anterior; p, posterior.

(C) Cell lineage reconstruction of the early *Drosophila* embryonic nervous system. The images show lateral and ventral views of 235 neural precursor cell tracks. Tracks are color coded for time (purple to yellow, 2.9–5.4 hr after egg laying). NB, neuroblast.

(D) Visualization of the results of a computational analysis of the dynamic cell behavior of different neuroblast (NB) types in the early *Drosophila* embryo. The analysis is based on the cell lineage reconstruction shown in (C). Using only morphodynamic features of tracked neuroblasts, such as spatiotemporal information about cell movements as well as timing and orientation of cell divisions during a period of 2 hr after the blastoderm stage, a machine learning classifier was built for automatically predicting the respective cell types. The figure panel shows a quantification of the accuracy of this machine learning classifier in the form of a confusion matrix. Manually annotated neuroblast types are arranged in columns; corresponding neuroblast types predicted by the machine learning classifier (without access to the manual annotation) are arranged in rows. Perfect prediction accuracy is indicated by a probability of 1 along the diagonal.

(E) Image segmentation using the atlas building pipeline by Heckscher et al. (2014). The image to the left shows a 3D rendering of a stage 16 CNS stained with anti-Even-skipped (Eve). Segments T2–A1 are shown (anterior upward, tilted ventral view). The image at the right shows the microscopy data after segmentation, using a random color code and representing each nucleus as a distinct object.

(F) Cell bodies of neurons and a subset of glia have predictable positions in the embryonic CNS. Images in the top row show maximum-intensity projections of microscopy data sets of in vivo transcription factor expression patterns (green, names at top) costained with Even-skipped (Eve, magenta). Coexpressing cells appear white. FlyBase full names: pMad, phospho-Mothers against Dpp; Dimm, Dimmed; Repo, Reversed polarity; Bar, BarH1/BarH2; Hb9, Extra-extra. Images in the bottom row show single-marker atlases constructed for each pair of markers shown in the top row.

(G) The image shows a rendering of all interneurons included in the eNeuro atlas. Each molecularly different subtype is represented by a different color (with, in total, 112 distinct molecular subtypes). Anterior is upward.

Scale bars, (A) 50 μm; (C) 20 μm; (F) 10 μm.

(A) through (D) were adapted from Amat et al. (2014). (E) through (G) were adapted with permission from Heckscher et al. (2014).

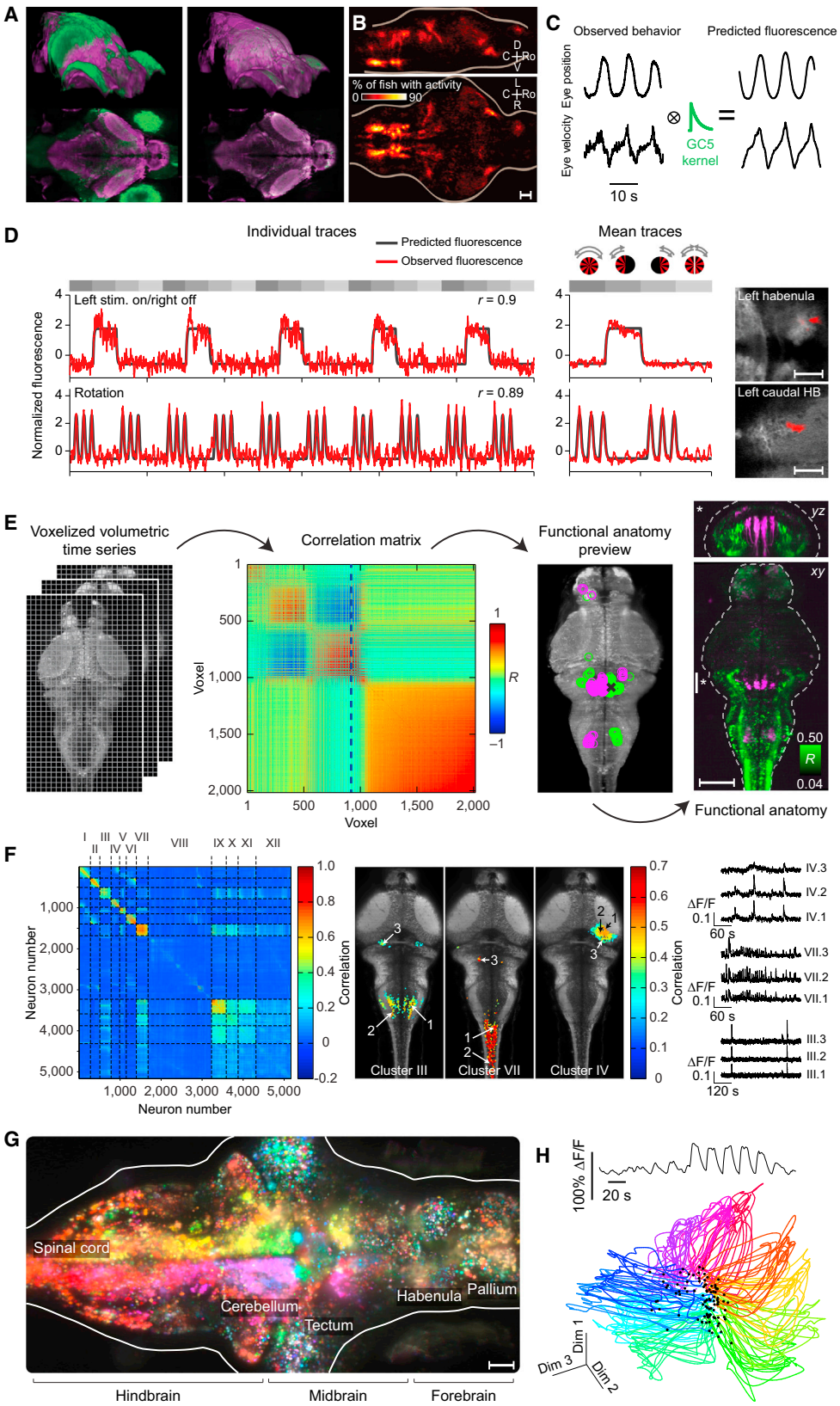

(legend on next page)

or univariate analysis, where activity of every voxel or neuron is expressed as a linear combination of the external variables (possibly convolved with a hypothesized calcium impulse response function) (Freeman et al., 2014; Friston et al., 2007; Miri et al., 2011; Portugues et al., 2014) or clustered into functional cell types according to responses to specific stimuli (Turaga and Holy, 2012). In a study by Portugues et al., whole-brain activity in zebrafish in response to moving visual scenes, acquired sequentially across planes with a two-photon microscope, was related to eye movements, tail movements, and sensory input, creating whole-brain functional maps of sensory representation and involvement in behavior (Figures 7A–7D). This technique was then followed by volumetric registration methods for combining such functional maps across multiple animals (Figures 7A–7D) to evaluate the consistency of the maps across brains.

In general, and especially for multivariate analyses that evaluate joint structure of activity across time and across neurons (e.g., principal component analysis and other correlation-based analyses) (Ahrens et al., 2013; Panier et al., 2013), processing large neural data sets often requires substantial computational resources (Figures 7E–7H). One approach to handing the scale of these data is to use distributed computing. Computer clusters, as present in many universities but also available online through services such as Amazon EC2, provide the ability to process large data sets within a short amount of time. In Freeman et al. (2014), an open-source analysis library called Thunder, built on the Apache Spark distributed computing platform, allows such large-scale computations to be run on private or publicly available clusters (Figures 7G and 7H). Algorithms in this modular, user-oriented library include mass-univariate regression, spatial and temporal factorizations, time series statistics, and others. Using these methods, brain maps could be generated that reveal relationships between whole-brain activity and sensory input and behavior, as well as temporal relationships between different populations across the brain. Complementing these brain maps were "dynamical portraits," which described the temporal evolution of brain activity in a lower dimensional space designed to capture essential structure in population dynamics. Many more developments in the analysis of large-scale network dynamics are likely to occur within computational neuroscience in the coming years.

What Is Large-Volume Imaging Good for?

As also recognized in the BRAIN initiative (Alivisatos et al., 2012), large-scale recordings are useful because they allow tackling of questions about network dynamics on a broader scale than typically addressed, including the following: how do populations in many spatially disparate regions interact, how does the state of one brain region affect the dynamics of other regions, and, how do sensory systems represent the world at the large network level? These are just a few routes along which large-scale recordings can make a difference (Figure 8).

Figure 7. Analysis of Whole-Brain Functional Imaging Data

(A) 3D volume registration across larval zebrafish brains. An individual brain (green) is morphed onto a reference brain (magenta) by performing an affine transformation, followed by nonrigid alignment. Left and right panels show the two brains before and after image registration.

(B) The percentage of fish (n = 13) imaged that show activity at each voxel (after registration) for all voxels within the brain, depicted as maximum projections from two orthogonal views.

(C) Sensory and motor signals are reflected in the measured activity. Behavioral and stimulus-related variables were convolved with an exponential kernel using the decay time constant of GCaMP5G. These convolved traces represented the predicted fluorescence that would be recorded if activity was related to each of those variables.

(D) Predicting region of interest (ROI) activity from behavioral variables. ROI activity is strongly correlated with the predicted fluorescence for different behavioral variables (regressors). For each example ROI, the fluorescence trace and the predicted fluorescence for the regressor with the highest correlation are shown. Left: normalized (Z score) fluorescence traces for a subset of stimulus (stim.) repetitions and the corresponding normalized (Z score) behavioral trace. The correlation coefficient is indicated. Center: normalized average fluorescence across stimulus repeats (and planes) for the ROI, with the corresponding normalized average behavioral trace. A schematic of the four stimuli is shown above the top center plot. Gray boxes indicate the duration of each of the four stimuli in all plots. Right: anatomical localization of the ROIs (red).

(E) Discovery of correlations in whole-brain light-sheet functional imaging data. The brain is first divided into supervoxels ($5 \times 5 \times 5\ \mu m^3$, approximate soma size) to reduce the data size, so that the supervoxel correlation matrix can be easily computed (first panel from the left). Clustering is performed on the correlation matrix by reordering the supervoxels according to the number of other supervoxels they are strongly correlated to (absolute value of correlation coefficient, >0.5); this reorders the columns to create a block-like matrix (second panel from the left). Next, within each block, one supervoxel is manually selected to generate a reference trace, which represents a dominant mode of activity captured by the block. After visualizing the positions of strongly correlated supervoxels (third panel from the left; green: strong positive correlations, >0.5; magenta: strong negative correlations, <−0.5), the reference trace is correlated to the signals from all voxels in the original data set, creating a full resolution volume of correlation coefficients (fourth panel from the left). The shown volume represents two independent sets of voxels from two clusters in the correlation matrix corresponding to highly correlated neurons and areas of neuropil (functional anatomy). The magenta set of voxels corresponds to the cluster indicated in the panel to the left.

(F) In a related method, neuronal regions of interest are first determined, after which activity is clustered using a correlation-based method. Left: correlation matrix of regions of interest, sorted with K-means clustering. Middle: anatomical layout of the neurons within three of the clusters. Right: examples of fluorescence time series from three neurons in the clusters shown.

(G) Direction tuning across the brain of larval zebrafish presented with moving whole-field visual stimuli in a setup that combines light-sheet imaging with visual stimulation and behavior (Vladimirov et al., 2014). The direction tuning maps are derived by fitting every voxel (with ~100 voxels per neuron) with a tuning-curve model that separately describes the temporal response profile and the tuning to direction. Color indicates preferred direction; saturation, tuning width (i.e., circular variance); brightness, response strength. White means responsive, but without unidirectional tuning. Image shows a dorsal maximum intensity projection through 39 planes covering 195 μm.

(H) Brain activity projected onto the first three components derived using regression and principal-component analysis, from a data set similar to that shown in (G). Every trace represents evolution of brain activity during one presentation of the moving visual stimulus (10 s motion, 10 s stationary). Color indicates stimulus direction. Black dots indicate trial (and stimulus) onset. The projections of brain activity separate according to stimulus direction, reflecting the different responses to different angles of visual motion. The trace represents the response of one neuron to 12 directions of visual motion.

Scale bars, (B and D) 50 μm; (E) 100 μm; and (G) 40 μm.

(A) through (D) were adapted with permission from Portugues et al. (2014). (E) was adapted with permission from Ahrens et al. (2013). (F) was adapted with permission from Panier et al. (2013). (G) and (H) were adapted from Freeman et al. (2014).

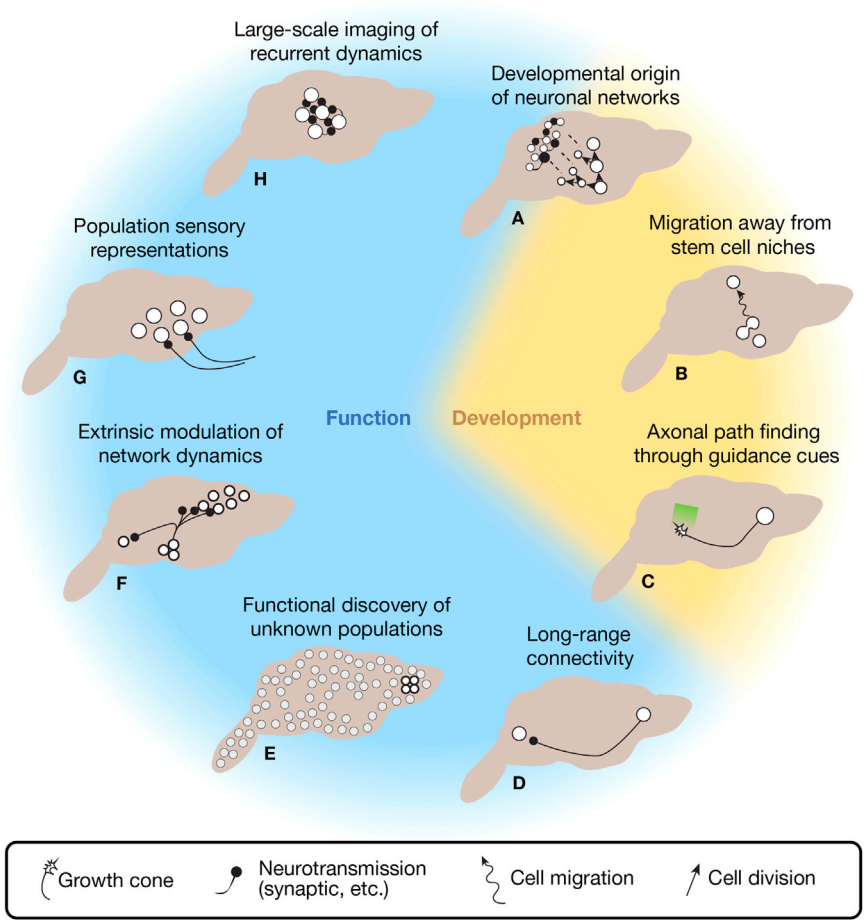

Figure 8. Applications of Large-Scale Nervous System Imaging

(A) During development, neurons arise from stem cells and divide further, eventually forming neuronal networks. Tracking these divisions and possibly imaging the emergence of connections would benefit from simultaneous imaging of growing populations of cells occupying larger and larger volumes.

(B) During development, neurons migrate within or even across brain areas (Brand and Livesey, 2011). Understanding how such migration gives rise to mature structures may require tracking cells across large volumes.

(C) Axonal path finding can be a spatially long-range process (Chao et al., 2009). Large-scale volumetric imaging is capable of visualizing the formation of multiple axons or large axonal structures simultaneously.

(D) Identifying correlations introduced by long-range synaptic connections (Hammer, 1993) becomes easier when imaging large volumes simultaneously.

(E) The existence of certain functionally defined neuron types may be hypothesized, but they might simply not have been found. Large-scale or whole-brain imaging increases the chances of discovering such hard-to-find populations.

(F) The understanding of how one population of neurons modulates activity in another, for example, through neuromodulation (Sara, 2009), benefits from simultaneous imaging of both populations.

(G) Representations of sensory information are often distributed over large populations of neurons (Seelig and Jayaraman, 2013) so that decoding, e.g., of visual scenes, requires the monitoring of many neurons at once.

(H) The understanding of dynamics of networks with recurrent connections (Hopfield, 1982) benefits from simultaneous measurement from many neurons, because the activity of each depends on the activity of many others.

One conceptual advantage is that, by increasing coverage, large-scale imaging reduces the number of hidden variables in a system. For instance, when making inferences about causal connections in neural networks or other systems, the common input problem often appears: if activity in two nodes is strongly related, it can be hard to differentiate the causal connections between them from a common, hidden, input to both (Nykamp, 2007). However, the more neurons recorded from, ideally, the entire brain, the larger the chance that this common input is included in the data and possibly can be identified through, for example, machine learning and post hoc anatomical tracing methods.

Similarly, in development, coverage is a straightforward way in which large-scale imaging may lead to insights into how the fine-scale dynamics eventually gives rise to the full complexity of a brain, how localized small-scale aberrations may lead to large-scale abnormalities, and how neurons migrate over potentially large distances to form brain areas.

Pairing large-scale imaging with perturbation techniques, such as optogenetics, will lead to insights greater than the sum of their parts. Currently, the effects of activating or silencing specified subpopulations are usually measured as changes in an animal's behavior (Witten et al., 2010) or changes in a restricted set of other neurons (Guo et al., 2009; Petreanu et al., 2007). With large-scale imaging, downstream effects of perturbations can be observed—within the limitations of the calcium sensor—at the global level, possibly linking observations of how a given perturbation affects behavior to those of how that perturbation alters brain-wide dynamics. This may also provide paths to strong inferences about patterns of functional connectivity.

Another avenue of synergy will be the combination of large-scale imaging and connectomics. Efforts in which measurements of neuron function are linked to reconstructed connectivity (Bock et al., 2011; Briggman et al., 2011) have made use of partial coverage by two-photon imaging and wider coverage of electron microscopy (EM) imaging, so that the connectivity of at least some of the imaged neurons can be determined. If large-scale EM would be combined with large-volume functional imaging, the direction can be reversed: one could start with the reconstruction of anatomical connectivity based on EM data and then extract the activity of connected neurons from the functional data. This type of strategy requires dense functional imaging of the entire reconstructed block of tissue; light-sheet microscopy and other methods of volumetric imaging will be invaluable for such studies.

Neural activity and genetic markers are, of course, not the only processes of interest, and imaging methods can equally be applied to, for example, glutamate release (Marvin et al., 2013), synapse formation (Livneh and Mizrahi, 2012), mRNA (Park et al., 2014), blood flow (Kleinfeld et al., 1998), and intracellular signaling (Nikolaev et al., 2006).

Outlook

Further advancements in imaging speed, spatial resolution, and the depth penetration of light microscopy are, of course, highly desirable. Despite the rapid progress we have seen with light-sheet microscopy over the past few years, imaging performance has not reached a plateau, and further breakthroughs can be expected.

Improving volumetric imaging speed will be crucial for resolving the fine dynamics of neural activity at the whole-brain level when using calcium indicators, and even more so in the realm of voltage imaging. Such improvements can be expected with further advances in camera technology—in particular, with the advent of next-generation sCMOS cameras—and can be complemented by advanced instrument designs incorporating, for instance, further parallelization of light-sheet illumination and wide-field fluorescence detection.

Improving imaging depth and spatial resolution in large, non-transparent specimens will be crucial for maximizing physical coverage of entire, small nervous systems, such as those of larval zebrafish or *Drosophila*, at the cellular or even subcellular level. Substantial improvements might arise through the use of adaptive optics (Bourgenot et al., 2012; Jorand et al., 2012; Turaga and Holy, 2013; Wang et al., 2014) in the illumination and detection arms of light-sheet microscopes and through the use of sophisticated microscope control software that systematically optimizes the microscope's optical degrees of freedom on the optically complex specimen itself, e.g., by adaptively focusing, positioning, and orienting the microscope's light sheets as a function of time and spatial location in the sample. Furthermore, depth penetration could be improved through the development and application of red-shifted calcium and voltage indicators with high sensitivity, brightness, and photostability.

Integrating high-speed volumetric imaging of nervous system function with the capability to perform fast and precise optical manipulation of the imaged volume will further enable the design of powerful new imaging assays for the systematic mapping of coarse functional connectivity and hypothesis testing. With more exhaustive imaging comes an increased chance of identifying the cell populations most crucial for a given behavior. In addition, pairing large-volume imaging with targeted cell activation may make it possible to form and test hypotheses in real time, in particular, if the required data analysis is implemented in an online fashion so that observation and perturbation can be performed in a single experiment.

Technological advances in imaging methods are ongoing, and synergies within and between optical and computational methods will push their capabilities ever further. Eventually, light microscopy may approach a limit where imaging methods no longer form a bottleneck; instead, tissue properties and molecular dynamics, which determine how much light a brain can tolerate, will become the limiting factor to speed, spatial coverage, and resolution. Until then, we expect many more exciting developments in volumetric light microscopy.

ACKNOWLEDGMENTS

We thank Timothy Dunn, Joseph Fetcho, Jeremy Freeman, Katie McDole, Minoru Koyama, Burkhard Höckendorf, James Truman, and the anonymous reviewers for valuable comments on the manuscript; the authors of Broxton et al. (2013), Dodt et al. (2007), Heckscher et al. (2014), Holekamp et al. (2008), Panier et al. (2013), Prevedel et al. (2014), Portugues et al. (2014), Quirin et al. (2014), Susaki et al. (2014), Tomer et al. (2014), and Wu et al. (2013) for kindly providing figure materials for reproduction in this work; and Logan Grosenick, Michael Broxton, and Karl Deisseroth for sharing figure materials prior to publication. This work was supported by the Howard Hughes Medical Institute.

REFERENCES

Ahrens, M.B., Orger, M.B., Robson, D.N., Li, J.M., and Keller, P.J. (2013). Whole-brain functional imaging at cellular resolution using light-sheet microscopy. Nat. Methods *10*, 413–420.

Alivisatos, A.P., Chun, M., Church, G.M., Greenspan, R.J., Roukes, M.L., and Yuste, R. (2012). The brain activity map project and the challenge of functional connectomics. Neuron *74*, 970–974.

Amat, F., Lemon, W., Mossing, D.P., McDole, K., Wan, Y., Branson, K., Myers, E.W., and Keller, P.J. (2014). Fast, accurate reconstruction of cell lineages from large-scale fluorescence microscopy data. Nat. Methods *11*, 951–958.

Anselmi, F., Ventalon, C., Bègue, A., Ogden, D., and Emiliani, V. (2011). Three-dimensional imaging and photostimulation by remote-focusing and holographic light patterning. Proc. Natl. Acad. Sci. USA *108*, 19504–19509.

Baumgart, E., and Kubitscheck, U. (2012). Scanned light sheet microscopy with confocal slit detection. Opt. Express *20*, 21805–21814.

Bock, D.D., Lee, W.-C.A., Kerlin, A.M., Andermann, M.L., Hood, G., Wetzel, A.W., Yurgenson, S., Soucy, E.R., Kim, H.S., and Reid, R.C. (2011). Network anatomy and in vivo physiology of visual cortical neurons. Nature *471*, 177–182.

Bourgenot, C., Saunter, C.D., Taylor, J.M., Girkin, J.M., and Love, G.D. (2012). 3D adaptive optics in a light sheet microscope. Opt. Express *20*, 13252–13261.

Brand, A.H., and Livesey, F.J. (2011). Neural stem cell biology in vertebrates and invertebrates: more alike than different? Neuron *70*, 719–729.

Briggman, K.L., Abarbanel, H.D., and Kristan, W.B., Jr. (2005). Optical imaging of neuronal populations during decision-making. Science *307*, 896–901.

Briggman, K.L., Helmstaedter, M., and Denk, W. (2011). Wiring specificity in the direction-selectivity circuit of the retina. Nature *471*, 183–188.

Broxton, M., Grosenick, L., Yang, S., Cohen, N., Andalman, A., Deisseroth, K., and Levoy, M. (2013). Wave optics theory and 3-D deconvolution for the light field microscope. Opt. Express *21*, 25418–25439.

Cao, G., Platisa, J., Pieribone, V.A., Raccuglia, D., Kunst, M., and Nitabach, M.N. (2013). Genetically targeted optical electrophysiology in intact neural circuits. Cell *154*, 904–913.

Chao, D.L., Ma, L., and Shen, K. (2009). Transient cell-cell interactions in neural circuit formation. Nat. Rev. Neurosci. *10*, 262–271.

Chen, T.W., Wardill, T.J., Sun, Y., Pulver, S.R., Renninger, S.L., Baohan, A., Schreiter, E.R., Kerr, R.A., Orger, M.B., Jayaraman, V., et al. (2013). Ultrasensitive fluorescent proteins for imaging neuronal activity. Nature *499*, 295–300.

Chung, K., Wallace, J., Kim, S.Y., Kalyanasundaram, S., Andalman, A.S., Davidson, T.J., Mirzabekov, J.J., Zalocusky, K.A., Mattis, J., Denisin, A.K., et al. (2013). Structural and molecular interrogation of intact biological systems. Nature *497*, 332–337.

Churchland, M.M., Cunningham, J.P., Kaufman, M.T., Foster, J.D., Nuyujukian, P., Ryu, S.I., and Shenoy, K.V. (2012). Neural population dynamics during reaching. Nature *487*, 51–56.

Denk, W., Strickler, J.H., and Webb, W.W. (1990). Two-photon laser scanning fluorescence microscopy. Science *248*, 73–76.

Dodt, H.U., Leischner, U., Schierloh, A., Jährling, N., Mauch, C.P., Deininger, K., Deussing, J.M., Eder, M., Zieglgänsberger, W., and Becker, K. (2007). Ultramicroscopy: three-dimensional visualization of neuronal networks in the whole mouse brain. Nat. Methods *4*, 331–336.

Dowski, E.R., Jr., and Cathey, W.T. (1995). Extended depth of field through wave-front coding. Appl. Opt. *34*, 1859–1866.

Fahrbach, F.O., and Rohrbach, A. (2012). Propagation stability of self-reconstructing Bessel beams enables contrast-enhanced imaging in thick media. Nat. Commun. *3*, 632.

Fahrbach, F.O., Simon, P., and Rohrbach, A. (2010). Microscopy with self-reconstructing beams. Nat. Photonics *4*, 780–785.

Freeman, J., Vladimirov, N., Kawashima, T., Mu, Y., Sofroniew, N.J., Bennett, D.V., Rosen, J., Yang, C.T., Looger, L.L., and Ahrens, M.B. (2014). Mapping brain activity at scale with cluster computing. Nat. Methods *11*, 941–950.

Friston, K.J., Ashburner, J., Kiebel, S.J., Nichols, T.E., and Penny, W.D. (2007). Statistical Parametric Mapping: the Analysis of Functional Brain Images. (Waltham: Academic Press).

Fuchs, E., Jaffe, J., Long, R., and Azam, F. (2002). Thin laser light sheet microscope for microbial oceanography. Opt. Express *10*, 145–154.

Gao, L., Shao, L., Higgins, C.D., Poulton, J.S., Peifer, M., Davidson, M.W., Wu, X., Goldstein, B., and Betzig, E. (2012). Noninvasive imaging beyond the diffraction limit of 3D dynamics in thickly fluorescent specimens. Cell *151*, 1370–1385.

Greenberg, D.S., Houweling, A.R., and Kerr, J.N. (2008). Population imaging of ongoing neuronal activity in the visual cortex of awake rats. Nat. Neurosci. *11*, 749–751.

Grewe, B.F., Langer, D., Kasper, H., Kampa, B.M., and Helmchen, F. (2010). High-speed in vivo calcium imaging reveals neuronal network activity with near-millisecond precision. Nat. Methods *7*, 399–405.

Grienberger, C., and Konnerth, A. (2012). Imaging calcium in neurons. Neuron *73*, 862–885.

Grosenick, L., Anderson, T., and Smith, S.J. (2009). Elastic source selection for in vivo imaging of neuronal ensembles. Proceedings of the 2009 6th IEEE International Symposium on Biomedical Imaging: From Nano to Macro. (New York: IEEE Press), pp. 1263–1266.

Grutzendler, J., Kasthuri, N., and Gan, W.B. (2002). Long-term dendritic spine stability in the adult cortex. Nature *420*, 812–816.

Guo, Z.V., Hart, A.C., and Ramanathan, S. (2009). Optical interrogation of neural circuits in Caenorhabditis elegans. Nat. Methods *6*, 891–896.

Hama, H., Kurokawa, H., Kawano, H., Ando, R., Shimogori, T., Noda, H., Fukami, K., Sakaue-Sawano, A., and Miyawaki, A. (2011). Scale: a chemical approach for fluorescence imaging and reconstruction of transparent mouse brain. Nat. Neurosci. *14*, 1481–1488.

Hammen, G.F., Turaga, D., Holy, T.E., and Meeks, J.P. (2014). Functional organization of glomerular maps in the mouse accessory olfactory bulb. Nat. Neurosci. *17*, 953–961.

Hammer, M. (1993). An identified neuron mediates the unconditioned stimulus in associative olfactory learning in honeybees. Nature *366*, 59–63.

Heckscher, E.S., Long, F., Layden, M.J., Chuang, C.H., Manning, L., Richart, J., Pearson, J.C., Crews, S.T., Peng, H., Myers, E., and Doe, C.Q. (2014). Atlas-builder software and the eNeuro atlas: resources for developmental biology and neuroscience. Development *141*, 2524–2532.

Holekamp, T.F., Turaga, D., and Holy, T.E. (2008). Fast three-dimensional fluorescence imaging of activity in neural populations by objective-coupled planar illumination microscopy. Neuron *57*, 661–672.

Holy, T.E., Dulac, C., and Meister, M. (2000). Responses of vomeronasal neurons to natural stimuli. Science *289*, 1569–1572.

Hopfield, J.J. (1982). Neural networks and physical systems with emergent collective computational abilities. Proc. Natl. Acad. Sci. USA *79*, 2554–2558.

Huisken, J., and Stainier, D.Y. (2007). Even fluorescence excitation by multidirectional selective plane illumination microscopy (mSPIM). Opt. Lett. *32*, 2608–2610.

Huisken, J., Swoger, J., Del Bene, F., Wittbrodt, J., and Stelzer, E.H.K. (2004). Optical sectioning deep inside live embryos by selective plane illumination microscopy. Science *305*, 1007–1009.

Jorand, R., Le Corre, G., Andilla, J., Maandhui, A., Frongia, C., Lobjois, V., Ducommun, B., and Lorenzo, C. (2012). Deep and clear optical imaging of thick inhomogeneous samples. PLoS ONE *7*, e35795.

Katona, G., Szalay, G., Maák, P., Kaszás, A., Veress, M., Hillier, D., Chiovini, B., Vizi, E.S., Roska, B., and Rózsa, B. (2012). Fast two-photon in vivo imaging with three-dimensional random-access scanning in large tissue volumes. Nat. Methods *9*, 201–208.

Keller, P.J. (2013). Imaging morphogenesis: technological advances and biological insights. Science *340*, 1234168.

Keller, P.J., and Dodt, H.U. (2012). Light sheet microscopy of living or cleared specimens. Curr. Opin. Neurobiol. *22*, 138–143.

Keller, P.J., Schmidt, A.D., Wittbrodt, J., and Stelzer, E.H.K. (2008). Reconstruction of zebrafish early embryonic development by scanned light sheet microscopy. Science *322*, 1065–1069.

Keller, P.J., Schmidt, A.D., Santella, A., Khairy, K., Bao, Z., Wittbrodt, J., and Stelzer, E.H. (2010). Fast, high-contrast imaging of animal development with scanned light sheet-based structured-illumination microscopy. Nat. Methods *7*, 637–642.

Kleinfeld, D., Mitra, P.P., Helmchen, F., and Denk, W. (1998). Fluctuations and stimulus-induced changes in blood flow observed in individual capillaries in layers 2 through 4 of rat neocortex. Proc. Natl. Acad. Sci. USA *95*, 15741–15746.

Kralj, J.M., Hochbaum, D.R., Douglass, A.D., and Cohen, A.E. (2011). Electrical spiking in Escherichia coli probed with a fluorescent voltage-indicating protein. Science *333*, 345–348.

Krzic, U., Gunther, S., Saunders, T.E., Streichan, S.J., and Hufnagel, L. (2012). Multiview light-sheet microscope for rapid in toto imaging. Nat. Methods *9*, 730–733.

Levoy, M., Ng, R., Adams, A., Footer, M., and Horowitz, M. (2006). Light field microscopy. ACM Trans. Graph. *25*, 924–934.

Levoy, M., Zhang, Z., and McDowall, I. (2009). Recording and controlling the 4D light field in a microscope using microlens arrays. J. Microsc. *235*, 144–162.

Lichtman, J.W., and Denk, W. (2011). The big and the small: challenges of imaging the brain's circuits. Science *334*, 618–623.

Lister, J.A., Robertson, C.P., Lepage, T., Johnson, S.L., and Raible, D.W. (1999). nacre encodes a zebrafish microphthalmia-related protein that regulates neural-crest-derived pigment cell fate. Development *126*, 3757–3767.

Livneh, Y., and Mizrahi, A. (2012). Experience-dependent plasticity of mature adult-born neurons. Nat. Neurosci. *15*, 26–28.

Madisen, L., Zwingman, T.A., Sunkin, S.M., Oh, S.W., Zariwala, H.A., Gu, H., Ng, L.L., Palmiter, R.D., Hawrylycz, M.J., Jones, A.R., et al. (2010). A robust and high-throughput Cre reporting and characterization system for the whole mouse brain. Nat. Neurosci. *13*, 133–140.

Mahou, P., Vermot, J., Beaurepaire, E., and Supatto, W. (2014). Multicolor two-photon light-sheet microscopy. Nat. Methods *11*, 600–601.

Majoul, I.V., Gao, L., Betzig, E., Onichtchouk, D., Butkevich, E., Kozlov, Y., Bukauskas, F., Bennett, M.V., Lippincott-Schwartz, J., and Duden, R. (2013). Fast structural responses of gap junction membrane domains to AB5 toxins. Proc. Natl. Acad. Sci. USA *110*, E4125–E4133.

Marvin, J.S., Borghuis, B.G., Tian, L., Cichon, J., Harnett, M.T., Akerboom, J., Gordus, A., Renninger, S.L., Chen, T.W., Bargmann, C.I., et al. (2013). An optimized fluorescent probe for visualizing glutamate neurotransmission. Nat. Methods *10*, 162–170.

Mertz, J. (2011). Optical sectioning microscopy with planar or structured illumination. Nat. Methods *8*, 811–819.

Mertz, J., and Kim, J. (2010). Scanning light-sheet microscopy in the whole mouse brain with HiLo background rejection. J. Biomed. Opt. *15*, 016027.

Miri, A., Daie, K., Burdine, R.D., Aksay, E., and Tank, D.W. (2011). Regression-based identification of behavior-encoding neurons during large-scale optical imaging of neural activity at cellular resolution. J. Neurophysiol. *105*, 964–980.

Muto, A., Ohkura, M., Abe, G., Nakai, J., and Kawakami, K. (2013). Real-time visualization of neuronal activity during perception. Curr. Biol. *23*, 307–311.

Nikolaev, V.O., Gambaryan, S., and Lohse, M.J. (2006). Fluorescent sensors for rapid monitoring of intracellular cGMP. Nat. Methods *3*, 23–25.

Nikolenko, V., Watson, B.O., Araya, R., Woodruff, A., Peterka, D.S., and Yuste, R. (2008). SLM microscopy: scanless two-photon imaging and photostimulation with spatial light modulators. Front. Neural Circuits *2*, 5.

Nykamp, D.Q. (2007). A mathematical framework for inferring connectivity in probabilistic neuronal networks. Math. Biosci. *205*, 204–251.

Palmer, A.E., and Tsien, R.Y. (2006). Measuring calcium signaling using genetically targetable fluorescent indicators. Nat. Protoc. *1*, 1057–1065.

Panier, T., Romano, S.A., Olive, R., Pietri, T., Sumbre, G., Candelier, R., and Debrégeas, G. (2013). Fast functional imaging of multiple brain regions in intact zebrafish larvae using selective plane illumination microscopy. Front. Neural Circuits *7*, 65.

Park, H.Y., Lim, H., Yoon, Y.J., Follenzi, A., Nwokafor, C., Lopez-Jones, M., Meng, X., and Singer, R.H. (2014). Visualization of dynamics of single endogenous mRNA labeled in live mouse. Science *343*, 422–424.

Petreanu, L., Huber, D., Sobczyk, A., and Svoboda, K. (2007). Channelrhodopsin-2-assisted circuit mapping of long-range callosal projections. Nat. Neurosci. *10*, 663–668.

Pfau, D., Pnevmatikakis, E.A., and Paninski, L. (2013). Robust learning of low-dimensional dynamics from large neural ensembles. C.J.C. Burges, L. Bottou, M. Welling, Z. Ghahramani, and K.Q. Weinberger, eds. Proceedings of Advances in Neural Information Processing Systems 26 (NIPS 2013), 1–9.

Planchon, T.A., Gao, L., Milkie, D.E., Davidson, M.W., Galbraith, J.A., Galbraith, C.G., and Betzig, E. (2011). Rapid three-dimensional isotropic imaging of living cells using Bessel beam plane illumination. Nat. Methods *8*, 417–423.

Portugues, R., Feierstein, C.E., Engert, F., and Orger, M.B. (2014). Whole-brain activity maps reveal stereotyped, distributed networks for visuomotor behavior. Neuron *81*, 1328–1343.

Prevedel, R., Yoon, Y.G., Hoffmann, M., Pak, N., Wetzstein, G., Kato, S., Schrödel, T., Raskar, R., Zimmer, M., Boyden, E.S., and Vaziri, A. (2014). Simultaneous whole-animal 3D imaging of neuronal activity using light-field microscopy. Nat. Methods *11*, 727–730.

Quirin, S., Jackson, J., Peterka, D.S., and Yuste, R. (2014). Simultaneous imaging of neural activity in three dimensions. Front. Neural Circuits *8*, 29.

Rohrbach, A. (2009). Artifacts resulting from imaging in scattering media: a theoretical prediction. Opt. Lett. *34*, 3041–3043.

Santi, P.A. (2011). Light sheet fluorescence microscopy: a review. J. Histochem. Cytochem. *59*, 129–138.

Sara, S.J. (2009). The locus coeruleus and noradrenergic modulation of cognition. Nat. Rev. Neurosci. *10*, 211–223.

Sasaki, T., Takahashi, N., Matsuki, N., and Ikegaya, Y. (2008). Fast and accurate detection of action potentials from somatic calcium fluctuations. J. Neurophysiol. *100*, 1668–1676.

Schmid, B., Shah, G., Scherf, N., Weber, M., Thierbach, K., Campos, C.P., Roeder, I., Aanstad, P., and Huisken, J. (2013). High-speed panoramic light-sheet microscopy reveals global endodermal cell dynamics. Nat. Commun. *4*, 2207.

Seelig, J.D., and Jayaraman, V. (2013). Feature detection and orientation tuning in the Drosophila central complex. Nature *503*, 262–266.

Siedentopf, H., and Zsigmondy, R. (1903). Über Sichtbarmachung und Größenbestimmung ultramikroskopischer Teilchen, mit besonderer Anwendung auf Goldrubingläser. Ann. Phys. *315*, 1–39.

Siegel, M.S., and Isacoff, E.Y. (1997). A genetically encoded optical probe of membrane voltage. Neuron *19*, 735–741.

Susaki, E.A., Tainaka, K., Perrin, D., Kishino, F., Tawara, T., Watanabe, T.M., Yokoyama, C., Onoe, H., Eguchi, M., Yamaguchi, S., et al. (2014). Whole-brain imaging with single-cell resolution using chemical cocktails and computational analysis. Cell *157*, 726–739.

Tomer, R., Khairy, K., Amat, F., and Keller, P.J. (2012). Quantitative high-speed imaging of entire developing embryos with simultaneous multiview light-sheet microscopy. Nat. Methods *9*, 755–763.

Tomer, R., Ye, L., Hsueh, B., and Deisseroth, K. (2014). Advanced CLARITY for rapid and high-resolution imaging of intact tissues. Nat. Protoc. *9*, 1682–1697.

Trachtenberg, J.T., Chen, B.E., Knott, G.W., Feng, G., Sanes, J.R., Welker, E., and Svoboda, K. (2002). Long-term in vivo imaging of experience-dependent synaptic plasticity in adult cortex. Nature *420*, 788–794.

Truong, T.V., Supatto, W., Koos, D.S., Choi, J.M., and Fraser, S.E. (2011). Deep and fast live imaging with two-photon scanned light-sheet microscopy. Nat. Methods *8*, 757–760.

Turaga, D., and Holy, T.E. (2012). Organization of vomeronasal sensory coding revealed by fast volumetric calcium imaging. J. Neurosci. *32*, 1612–1621.

Turaga, D., and Holy, T.E. (2013). Aberrations and their correction in light-sheet microscopy: a low-dimensional parametrization. Biomed. Opt. Express *4*, 1654–1661.

Vladimirov, N., Mu, Y., Kawashima, T., Bennett, D.V., Yang, C.T., Looger, L.L., Keller, P.J., Freeman, J., and Ahrens, M.B. (2014). Light-sheet functional imaging in fictively behaving zebrafish. Nat. Methods *11*, 883–884.

Vogelstein, J.T., Packer, A.M., Machado, T.A., Sippy, T., Babadi, B., Yuste, R., and Paninski, L. (2010). Fast nonnegative deconvolution for spike train inference from population calcium imaging. J. Neurophysiol. *104*, 3691–3704.

Voie, A.H., Burns, D.H., and Spelman, F.A. (1993). Orthogonal-plane fluorescence optical sectioning: three-dimensional imaging of macroscopic biological specimens. J. Microsc. *170*, 229–236.

Wang, K., Milkie, D.E., Saxena, A., Engerer, P., Misgeld, T., Bronner, M.E., Mumm, J., and Betzig, E. (2014). Rapid adaptive optical recovery of optimal resolution over large volumes. Nat. Methods *11*, 625–628.

Weber, M., and Huisken, J. (2011). Light sheet microscopy for real-time developmental biology. Curr. Opin. Genet. Dev. *21*, 566–572.

Winter, P.W., and Shroff, H. (2014). Faster fluorescence microscopy: advances in high speed biological imaging. Curr. Opin. Chem. Biol. *20*, 46–53.

Witten, I.B., Lin, S.C., Brodsky, M., Prakash, R., Diester, I., Anikeeva, P., Gradinaru, V., Ramakrishnan, C., and Deisseroth, K. (2010). Cholinergic interneurons control local circuit activity and cocaine conditioning. Science *330*, 1677–1681.

Wu, Y., Ghitani, A., Christensen, R., Santella, A., Du, Z., Rondeau, G., Bao, Z., Colón-Ramos, D., and Shroff, H. (2011). Inverted selective plane illumination microscopy (iSPIM) enables coupled cell identity lineaging and neurodevelopmental imaging in Caenorhabditis elegans. Proc. Natl. Acad. Sci. USA *108*, 17708–17713.

Wu, Y., Wawrzusin, P., Senseney, J., Fischer, R.S., Christensen, R., Santella, A., York, A.G., Winter, P.W., Waterman, C.M., Bao, Z., et al. (2013). Spatially isotropic four-dimensional imaging with dual-view plane illumination microscopy. Nat. Biotechnol. *31*, 1032–1038.

Yaksi, E., and Friedrich, R.W. (2006). Reconstruction of firing rate changes across neuronal populations by temporally deconvolved Ca2+ imaging. Nat. Methods *3*, 377–383.

Yu, B.M., Kemere, C., Santhanam, G., Afshar, A., Ryu, S.I., Meng, T.H., Sahani, M., and Shenoy, K.V. (2007). Mixture of trajectory models for neural decoding of goal-directed movements. J. Neurophysiol. *97*, 3763–3780.